ABSTRACT

Title of Thesis:	METHODS IN REALISTIC COMPUTATIONAL MODELING OF THE AVIAN NUCLEUS LAMINARIS
Degree candidate:	Victor Grau Serrat
Degree and year:	Master of Science, 2003
Thesis directed by:	Professor Jonathan Z. Simon Department of Electrical and Computer Engineering

On the basis of a previous model of coincidence detection neurons of nucleus laminaris (NL) in the auditory brainstem, a biophysically more realistic implementation was developed. The aim of the model was to faithfully characterize the diversity of cells observed within the nucleus, and account for their tonotopic arrangement. Anatomical and electrophysiological data was compiled and distilled from the literature. Due to the scarcity of experimental data and the high level of detail sought, a large set of parameters loosely defined a huge variable space. The biological relevant subspace was found by combining the biological constraints with a brute force exploration in a distributed environment. The result is a method that accurately described the high frequency cells of NL. Important physiological divergences between modeled cells within the nucleus, which result from reported anatomical differences, are discussed. The varying morphology of the cells seems to impose underestimated constraints on the physiology of the cells throughout the tonotopic axis of NL. Physiological gradients are considered as possible explanations to unexpected outcomes of the model, arguing their limited effect.

METHODS IN REALISTIC COMPUTATIONAL MODELING OF THE AVIAN NUCLEUS LAMINARIS

by

Victor Grau Serrat

Thesis submitted to the Faculty of the Graduate School of the
University of Maryland, College Park in partial fulfillment
of the requirements for the degree of
Master of Science
2003

Advisory Committee:

Professor Jonathan Z. Simon, Chair
Professor Catherine E. Carr
Professor Shihab A. Shamma

ACKNOWLEDGEMENTS

To Jonathan Z. Simon,

You cannot teach a man anything,
you can only help him find it for himself. Galileo Galilei

To Catherine E. Carr,

One of the advantages of being disorderly is that
one is always making new and exciting discoveries. A. A. Milne

To Kate MacLeod,

Who does not understand a glance,
cannot understand a long explanation. Arab proverb

To Shantanu Ray,

What is a friend?
A single soul dwelling in two bodies. Aristotle

To the rest of the crew of CSSL and NSL who helped me in ways small and large, but above all have made this thesis enjoyable. Finally, my parents have always taught me to be thankful. Thus, special thanks goes to myself, without whom this thesis would certainly not have been possible.

It's the possibility of having a dream
come true that makes life interesting. *The Alchemist*, P. Coelho

TABLE OF CONTENTS

LIST OF TABLES

LIST OF FIGURES

Chapter 1

Introduction

Computational neuroscience is a discipline that aims to understand how information is processed in the nervous system by developing formal models at many different structural scales. Using a multidisciplinary approach, the biological systems are modeled incorporating the constraints imposed by psychophysical, neurobiological and formal computational analyses. In order to fully comprehend the very diverse and highly specialized tasks of the nervous systems, multiple levels of analysis have to be addressed ranging from detailing the biophysical mechanisms responsible for these computations to evaluating the overall system performance.

The end product of computational analysis should be a sufficiently specified model, internally consistent, and complete enough to enable formal mathematical characterization or computer simulation. Such properties ensure that the computed outcome accurately reproduces the functions of the modeled system. Often is the case that specific features of the real world are not fully understood by the modeler, who therefore must guess about them when designing and testing the model. Conjectures are to be made, notwithstanding, following psychophysical and neurobiological constraints, as the theoretical outcomes of the

model would otherwise fail to capture the nature of biological computation. A certain degree of ignorance about the real phenomenon is implicit in the modeling process, because it is indeed the aim of such a process to gain a deeper insight into the mechanisms governing the object of study.

1.1 Auditory computation

Characterized by processing information about two orders of magnitude faster than the rest of the brain, the auditory system is responsible for providing a representation of the pattern of incoming sound signals, and specifying the locations of the corresponding sound sources relative to the listener. Specifically, sound localization is computed by means of interaural temporal and level differences over the entire spectrum of the signal from the sound coming to both ears.

The picture of what is accomplished in the brain stem auditory nuclei as acoustic information ascends the auditory pathway is still fragmentary, but there is no doubt that auditory neurons are specialized for precisely timed electrical signaling. Despite some similarities in the organization of the brain stem auditory nuclei between diverse animal classes, the avian system is regarded as having a simpler structure and the function of each nucleus involved is better understood than the mammalian analog [27, 39]. The present study focuses exclusively on sound localization in avians.

Timing information in sound is captured in the cochlea and is conveyed to the auditory nerve, which projects to the cochlear nuclei. One branch of the auditory nerve innervates nucleus angularis (NA) and another innervates nucleus magnocellularis (NM), whose afferents project to nucleus laminaris (NL).

Evidence is accumulating that many neurons in NA are specialized for intensity analysis of complex sounds, whereas NM and NL are adapted for analysis of interaural time differences (ITDs) [39]. Detection and computation of ITDs is the underlying mechanism used in azimuthal sound localization in the brain.

The most prominent and important model of binaural interaction was suggested by Jeffress [18] as a mechanism for sensitivity to interaural time delays. The model postulates the existence of neuronal fibers that contain temporal information about the waveform of the acoustic stimulus in their discharge pattern. These fibers project with ladder-like branching patterns to cells in a binaural nucleus that only discharge when receiving coincident spikes from their monoaural afferents. The lengths of the mentioned fibers are supposed to introduce internal neuronal delays that compensate for the acoustic delay of incoming signals between both ears. The model suggests the computation of ITDs by means of delay lines and coincidence detectors, transforming a time code into a space code.

Anatomical and physiological evidence shows that the cochlear nucleus is the likely site of Jeffress' model: nucleus magnocellularis axons are hypothesized to work as delay lines, and nucleus laminaris cells are thought to play the role of coincidence detectors [3, 28]. Nucleus laminaris is mainly composed by cells that extend their dendrites dorsally and ventrally in a bipolar fashion. Each cluster of dendrites receives inputs from one ear: the ipsilateral NM projects onto the dorsal side, whereas the contralateral NM innervates the ventral side. Additionally, neurons within both nuclei are arranged tonotopically: their neuronal location depends on the frequency band to which they are tuned.

1.2 Motivations and objectives

In nucleus laminaris, a strong functional hypothesis can be formulated and biological data can be feasibly obtained from experiments *in vitro*. As a result, NL has already been the objective of many anatomical [9, 10, 11, 38, 43, 44] and electrophysiological experiments [3, 23, 28, 36, 47], as well as the target of some computer modeling efforts. Previous models have yielded significant results in explaining some particular features of NL: the role of dendrites in auditory coincidence detection [1], phase locking capabilities and synaptic location [42] and short-term synaptic plasticity as an adaptive mechanism for preserving ITD information [6].

Whereas anatomical data roughly covers the entire nucleus laminaris, physiological data tends to be recorded from the high frequency region of the nucleus. The outlined computational models, which are built on the experimental data available, are therefore restricted to the same neuronal zones. Instead of concentrating on the variability of features observed within the nucleus, some degree of uniformity is assumed between cells, and the results are subsequently generalized to the whole.

Merging previous approaches with the reported morphological gradients of the cells under study, the present work intends to provide a broader description, coherent with the varied amount of biological data available. The main goal of this study is to construct a biophysically realistic model of neuronal coincidence detection within the framework of an existing model of nucleus laminaris [42]. A neuron-level approach is aimed at faithfully characterizing the morphology, electrical properties and channel dynamics that underlie the characteristic behavior of nucleus laminaris cells.

While seeking to account for the variability observed between cells within the nucleus and gain deeper understanding of their specialization, a biophysically coherent description of the entire nucleus is the goal of the modeling efforts to ultimate unveil the intricacies of neuronal coincidence detection. The cost of the intended level of detail is, from a modeling point of view, an increase in the number of parameters. Despite the significant sources of information, the variable space of the model is not tightly constrained. An exhaustive exploration of all possible combinations is thus unconceivable. Instead, a strategic scattered examination is performed taking advantage of the available computer resources in a distributed system.

Within this operational framework, the relation between biology and computer modeling is conceived to be bidirectional. Experimental data is the basis upon which the model is built, and the end product of the model are predictions that can be used to guide future experiments.

Chapter 2

Modeling background

Electrical signals are the basis of information transfer in the nervous system. Nerve cells have evolved elaborate mechanisms for generating and processing electrical signals based on the flow of ions across their plasma membranes. Biological membranes exhibit distinctive features similar to those of electrical circuits, and this analogy is the basis for describing and modeling the behavior and functionality of nerve cells: neurons are often described in terms of their equivalent circuits.

The cornerstone of any biophysically realistic neuronal model is the point representation of the cell, where the morphology of the neuron is reduced to a single point or compartment. The specialization of the plasma membrane to deal with electrical signals makes it permeable to some ion species but not to others. Therefore, a separation of charge normally occurs across the membrane: there is a difference between the intracellular (V_i) and extracellular (V_o) potentials, termed the membrane potential (V_m):

$$V_m = V_i - V_o \tag{2.1}$$

In particular, at rest, all cells have a negative resting potential (V_{rest}). The

isolation properties of the membrane are well described with a capacitor (C), and the membrane permeability can initially be described with a resistor (R): the current that flows through the membrane bears a linear relation with the voltage across the membrane, following Ohm's law. These three elements constitute the equivalent circuit of the passive membrane as depicted in Figure 2.1.

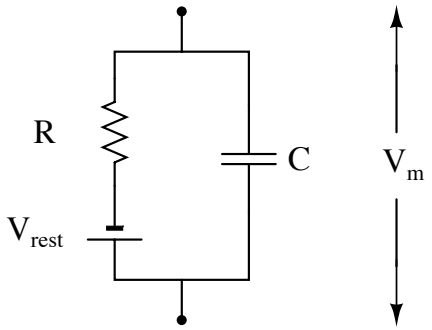

Figure 2.1: Equivalent circuit of the point representation of a neuron.

For a full review on Sections 2.1 and 2.2, the reader is referred to [19, 21].

2.1 Linear cable theory

The vast majority of neurons present a much more complicated structure than a single compartment spherical cell. In general, neurons have extensive dendritic trees that receive a myriad of excitatory and inhibitory synaptic inputs. These extended systems have a cablelike structure. Consequently, the dynamics of the membrane potential along them are governed by linear cable theory, in which the electrical properties of a given system are analyzed in relation to its specific cylindrical geometry. Many parts of a neuron can be approximated by a cylinder, characterized by a conductive core surrounded by a membrane that has different electrical properties from its core. The analogy with a standard copper wire is

the foundation for extending the mathematical description of the current flow through the wire to the flow of ions through neuronal fibers.

The relation between current and voltage in one-dimensional cable is described by the cable equation, a partial differential equation, first order in time and second order in space. Three basic assumptions are made to derive it: the membrane parameters are assumed to be linear and uniform throughout the fiber; current flows only along a single spatial dimension, the length of the cable (radial current is zero); for convenience, the extracellular resistance is assumed to be zero. In order to numerically solve the cable equation, a spatial discretization of the cable into different segments is performed, which results in a family of differential equations, one for each segment. Figure 2.2 depicts the single passive cable, formed by a set of connected compartments or segments. Each compartment is the point representation of the passive membrane described in the previous section. This more elaborate model incorporates the intracellular cytoplasm, modeled as a resistor (R_i) that connects adjacent compartments.

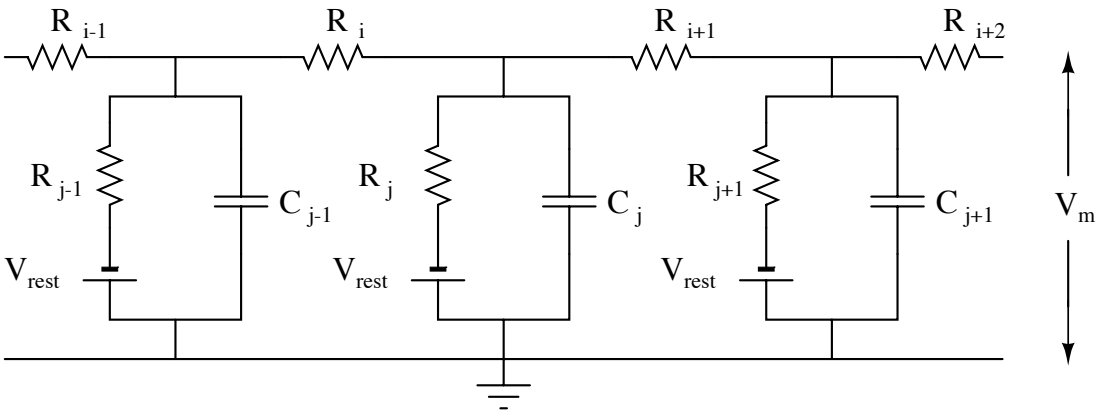

Figure 2.2: Equivalent circuit of a neuronal fiber.

Within the cable theory framework, Rall [33] proposed that any neuronal

dendritic tree could be simplified to a single equivalent cable with regard to its electrical properties. Two additional assumptions are made to those of the cable theory. Firstly, at any branch point, the parent cable diameter (d_0) relates to that of its daughters (d_i) by the relation:

$$d_0^{3/2} = \sum_i d_i^{3/2} \tag{2.2}$$

Secondly, all terminal branches end at the same electrotonic distance from the origin in the main branch. Real dendritic trees rarely conform to these assumptions. Nonetheless, this simplification is often accepted to model complex dendritic arborizations as a first approach to explain the contribution of the dendrites, while avoiding the burden of detailing their involved geometry.

2.2 Hodgkin and Huxley channel types

The primary electrical signal generated by nerve cells is the action potential, which results from a change in membrane permeability to specific ions. Hodgkin and Huxley [17] set the foundation to mathematically describe and quantify the kinetics governing the generation of action potentials. They postulated a phenomenological model based on their experiments in the squid giant axon.

Two independent major voltage-dependent ionic conductances, a sodium conductance G_{Na} and a potassium conductance G_K, are involved in the generation of the action potential. Additionally, there is a third smaller conductance, termed leak (G_{leak}), that does not depend on the membrane potential. Each conductance has a reversal potential associated with it given by Nernst's equation for the corresponding ion type, which depends on the different extracellular and intracellular ion concentrations. The point model of the neuron

is thereby extended to accommodate the sodium and potassium permeabilities as depicted in Figure 2.3, where the resistors are named by their inverses, the conductances.

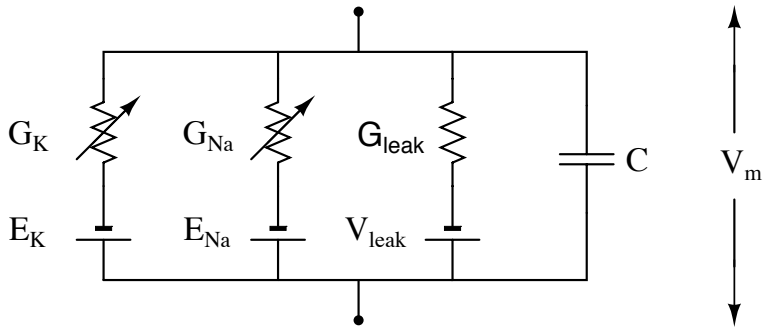

Figure 2.3: Hodgking and Huxley model of the neuronal membrane.

Both G_{Na} and G_K are expressed in terms of a maximum conductance ($\overline{G_{Na}}$ and $\overline{G_K}$) multiplied by a numerical coefficient that represents the fraction of the maximum conductance open at a given time. This coefficient is seen as a gating variable that switches between its two possible states: permissive or open, and nonpermissive or closed. The transition between both states is governed by first-order kinetics, and, for the potassium case, it can be written as:

$$n \underset{\alpha_n}{\overset{\beta_n}{\rightleftharpoons}} 1 - n \tag{2.3}$$

where n is the probability that the gate is open, and 1-n is the probability of being closed. α_n and β_n are voltage-dependent rate variables (in units of s^{-1}) that specify how many transitions occur between the closed and open states and vice versa. Mathematically, this scheme translates into a first-order differential equation of the form:

$$\frac{dn}{dt} = \alpha_n(V)(1-n) - \beta_n(V)n \tag{2.4}$$

where V is the membrane potential of the neuron. Eq. 2.4 yields the following solution:

$$n(t) = n_0 - \left[(n_0 - n_\infty)\left(1 - e^{-t/\tau_n}\right)\right] \tag{2.5}$$

$$n_\infty = \frac{\alpha_n}{\alpha_n + \beta_n} \tag{2.6}$$

$$\tau_n = \frac{1}{\alpha_n + \beta_n} \tag{2.7}$$

Hodking and Huxley parametrized the dependence of α and β with the membrane potential as follows (expressed in the most general form):

$$\alpha_n(V) = \frac{\alpha_{n0}(\frac{V - \alpha_{nV_{1/2}}}{\alpha_{nk}})}{1 - e^{\frac{\alpha_{nV_{1/2}} - V}{\alpha_{nk}}}} \tag{2.8}$$

$$\beta_n(V) = \beta_{n0} e^{\frac{\beta_{nV_{1/2}} - V}{\beta_{nk}}} \tag{2.9}$$

where $\alpha_{nV_{1/2}}$ and $\beta_{nV_{1/2}}$ are the midpoints for activation and deactivation, α_{nk} and β_{nk} define the voltage range in which activation and deactivation takes place, and α_{n0} and β_{n0} give the slope of activation and deactivation. To sum up, the current that will flow across the plasma membrane through the potassium channels (I_K) is expressed as:

$$I_K = \overline{G_K} n^4 (E_K - V) \tag{2.10}$$

where the power to the 4 of n indicates that there are 4 independent variables (required to account for the observed kinetics), and the joint probability of the channel being open or closed is the product of each single probability. E_K is the reversal potential for potassium.

The description of the dynamics of the sodium conductance are slightly more complex. In order to fit the kinetics of the sodium current, Hodgkin and Huxley

had to postulate the existence of a sodium activation variable m and a sodium inactivation variable h. As a result, the sodium analogous equation of Eq. 2.10 is:

$$I_{Na} = \overline{G_{Na}} m^3 h (E_{Na} - V) \tag{2.11}$$

Similar to before, the temporal evolution of m and h is governed by the corresponding first-order differential equations, for whose solution Hodgkin and Huxley empirically derived the following equations for the rate variables (expressed in the most general form):

$$\alpha_m(V) = \frac{\alpha_{m0}(\frac{V-\alpha_{mV_{1/2}}}{\alpha_{mk}})}{1 - e^{\frac{\alpha_{mV_{1/2}}-V}{\alpha_{mk}}}} \tag{2.12}$$

$$\beta_m(V) = \beta_{m0} e^{\frac{\beta_{mV_{1/2}}-V}{\beta_{mk}}} \tag{2.13}$$

$$\alpha_h(V) = \alpha_{h0} e^{\frac{\alpha_{hV_{1/2}}-V}{\alpha_{hk}}} \tag{2.14}$$

$$\beta_h(V) = \frac{\beta_{h0}}{1 + e^{\frac{\beta_{hV_{1/2}}-V}{\beta_{hk}}}} \tag{2.15}$$

This set of equations gives a quantitative account for voltage- and time-dependent sodium and potassium conductances, and fully describes the waveforms of action potentials. Figure 2.4 shows the time plots that correspond to a current injection of 0.5 ms in duration and 0.4 nA in amplitude to the equivalent circuit represented in Figure 2.3. For this plot, all parameters are set equal to those reported in the original paper [17].

2.3 The NEURON environment

Information processing in the brain results from complex changes of membrane properties constrained to operate within the limitations of the intricate anatomy

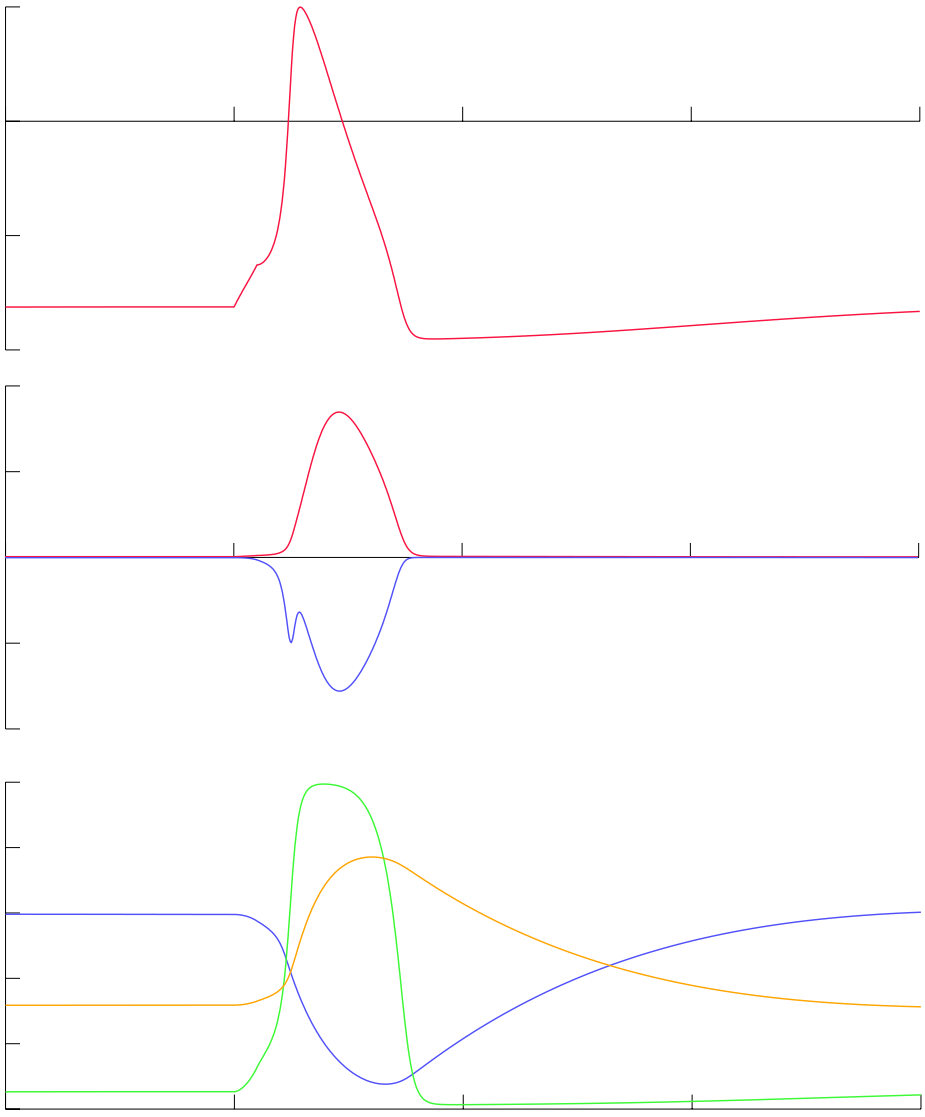

Figure 2.4: Hogkin and Huxley action potential. Computed action potential in response to a 0.5 ms current pulse of 0.4 nA. The upper graph shows the evolution of the membrane potential. The middle graph shows the potassium and sodium currents, and the lower graph plots the evolution of the gating particles n, m, and h.

of neurons. As outlined in previous sections, the mathematical framework used to describe such brain mechanisms usually consists of a large set of equations that generally do not have analytical solutions. In most of the cases, because of the nonlinearities and spatiotemporal complexities of such equations, intuition does not provide much help in understanding the cells' behavior. Nonetheless, having defined the set of algebraic equations, it can easily be solved numerically by using the appropriate computational tools. NEURON is such a tool that provides a flexible environment for implementing biologically realistic models of electrical and chemical signaling in neurons and networks of neurons [14]. Specifically designed to simulate nerve cells, NEURON allows the user to deal directly with concepts at the neuroscience level, provides with a customizable graphical user interface (GUI) and is particularly efficient because of the use of special methods that take advantage of the structure of nerve equations [13].

Spatiotemporally continuous variables are computed over a set of discrete points in space, called nodes, for a finite number of instants in time. NEURON allows for a conceptual division of the different parts of the cell into different cable sections, which can be connected together to form any branched structure. Each section can be divided into $nseg$ segments, whose midpoints are the mentioned nodes. Using the second order integration method provided by NEURON (a variant of Crank-Nicholson), the discrete solutions are a piecewise linear approximation to the continuous system with second order accuracy proportional to Δt^2, where Δt is the chosen time step. The size of Δt and the fineness of the spatial grid jointly determine the accuracy of the solution. Therefore, a tradeoff must be met between spatiotemporal accuracy and computational efficiency. The spatial grid was chosen by repeatedly increasing

the number of grid points (by tripling them, [16]) until further increases caused no significant change in simulation results. Accordingly, *nseg* is set to 9 in all sections, except for the axon node that is already small enough and *nseg* is set to 1 (cf. Section 3.1). Depending on the types of simulations to be run, the performance of the integration method can be changed in the model by using a fixed or an adaptive time step. If a fixed time step is chosen, Δt is set by default at 0.0125 ms, being more than one order of magnitude smaller than the time constant for the faster events to be simulated (e.g. mean half-width of an action potential is around 0.3 ms). For the adaptive case, the specification comes in terms of an absolute error rather than Δt. A maximum absolute error of 0.01 in the adaptative case and Δt=0.0125 ms for the fixed time step yield similar degrees of accuracy [16].

NEURON incorporates a programming language based on Hoc [20], a floating point calculator with C-like object oriented syntax that can be used to implement abstract data types. The starting point for the present work is a previous model of nucleus laminaris written in Hoc: about 7500 lines (100 pages) of code that construct an array of cells in nucleus laminaris with a high degree of customization and an adapted GUI designed to test and evaluate the performance of the modeled cells [42]. Additionally, NEURON incorporates a high-level language (NMODL [15]) for incorporating new biophysical mechanisms in models. NMODL offers a syntax that closely resembles familiar mathematical and chemical notation. NMODL files are automatically translated into C and further compiled for computational efficiency. The channels and synaptic mechanisms embodied in the model are customized using this language.

2.4 Distributed simulations

A great level of detail in the model is required to accomplish the ultimate goal of making it biophysically realistic. Almost one hundred different parameters are needed to accurately model the morphology of the cell, the kinetics of the channels involved, and the variety of the stimuli delivered. Consequently, the resulting parameter space is intractably huge, even though only a small volume of this space is biologically relevant. Experimental data imposes an important constraint on defining the initial space to be searched. However, due to the limited empirical data available, it is still unfeasible to ransack the constrained space in order to locate where the biologically significant subspace lies.

In order to maximize the chances of successfully pursuing the parameter search, a system was devised to automatically explore different sets of points in a given subspace. This process is carried out by a program written in Perl that continuously performs three main tasks: it progressively generates all possible combinations that result from a given reduced set of parameters; it distributes each combination among a pool of available machines for its simulation; it processes the outcome of each simulation by either saving the combination if it matches a given criterion or discarding it otherwise. A brute force approach is employed to compensate for the uncertainty about the size and continuity of the possible solution space. The program runs asynchronously, it is fault tolerant and crash resistant, and can run for several days. By distributing the simulations among an average of 20 workstations, the program takes great advantage from the available university computing facilities in an inherent distributed environment such as the Unix system in the Glue project (cf. http://www.glue.umd.edu). Slightly less than a linear factor decrease in the

overall running time is achieved through the distribution process (e.g. a factor of 3.5 with 5 machines, independent of the number of simultaneous simulations per machine). It cannot compensate for the exponential increase in the number of simulations (as a function of their quantity and depth), but it still provides a very powerful scanning tool.

Chapter 3

Initial implementation

The modeling process starts by dissecting the object of study into its constituent parts. The initial specifications for each of the components consists in assigning the appropriate level of detail to each section. A tradeoff between biological accuracy and computational efficiency is implicit throughout the whole process.

Anatomical and electrophysiological data is collected from surveying the available literature. Experimental data sets the foundations for characterizing each modeled section in accordance to the observed features of real cells (cf. Figure 3.1). The choices for each parameter are discussed herein in order to provide a preliminary notion about their estimated relevance.

3.1 Morphology

The preponderant neuron in nucleus laminaris is generally characterized by a cylindrical, ellipsoid or ovoid cell soma, which is spineless. The diameter of the soma is between 15 μm and 20 μm [30, 43, 44] and the size of the somata remains relatively constant throughout the nucleus. The length of the soma is in the same range of values as the diameter.

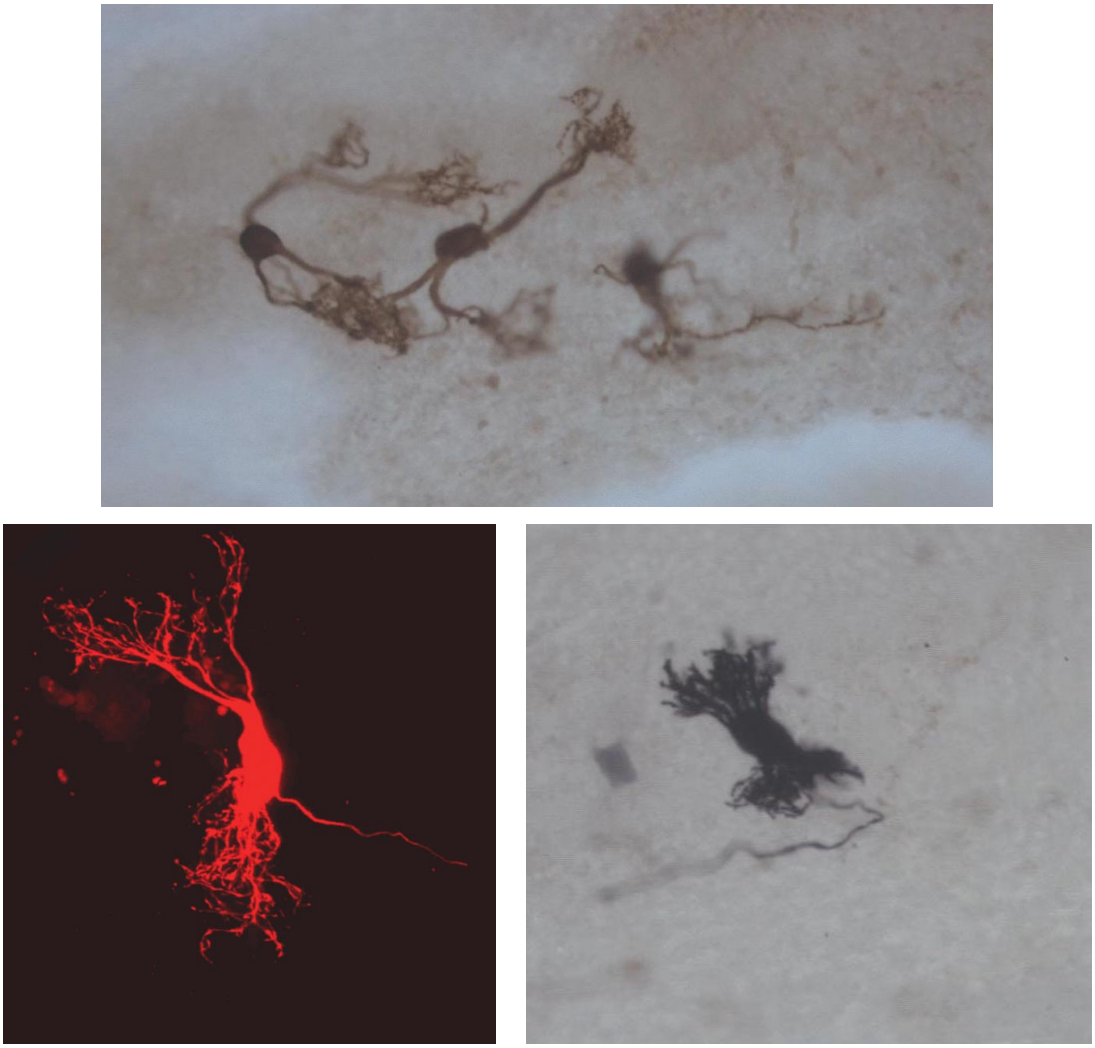

Figure 3.1: Biocytin filled nucleus laminaris neurons from the chicken. Low frequency (top), mid frequency (bottom left) and high frequency cells (bottom right). Photographs courtesy of Kate MacLeod and Catherine E. Carr.

The somatic region in the model is a truncated ovoid, and is formed by the revolution of a half period sinusoidal profile about the major axis of the cell:

$$d(x) = (d_{max} - d_{min})sin(\pi x) + d_{min} \tag{3.1}$$

where $d(x)$ is the cell diameter as a function of the position parameter x. NEURON defines the position in each compartment in the range $0 \leq x \leq 1$ from one end to the other [14]. d_{max} is set to 20 μm and d_{min} is set to 10 μm [11]. The sine function is chosen for being continuous and derivable to ensure the smoothness reported in the shape of real cells. The length of the somatic compartment, L_{soma}, is set to 20 μm.

The most important feature of the soma shape is its corresponding surface area. All membrane properties that characterize the cell are defined in the model in terms of concentrations per unit area. Thus, the membrane mechanisms placed in the soma will be a function of the total somatic external membrane. The associated area for the modeled soma can be calculated as:

$$Area_{ideal} = \int_0^L 2\pi d\Big(\frac{x}{L_{soma}}\Big)\sqrt{1 + d'\Big(\frac{x}{L_{soma}}\Big)^2} \tag{3.2}$$

which results in a total area of 1066 μm^2. However, the effective area computed by NEURON will differ as a result of the spatial discretization of the soma into $nseg$ different segments (where $nseg$=9, cf. Section 2.3), as depicted in Figure 3.2. The effective area will be the sum of the areas of the $nseg$ cylinders, whose diameter is obtained by evaluating Eq. 3.1 at the midpoint of each segment:

$$Area_{effective} = \sum_{i=0}^{nseg-1} 2\pi \frac{L_{soma}}{nseg} d\Big(x\Big|_{x=\frac{L_{soma}}{nseg}\left(\frac{1}{2}+i\right)}\Big) \tag{3.3}$$

Therefore, the effective area is 1030 μm^2. Either of these areas is consistent with the data from the literature: their planar projection (Area/π: 339 and

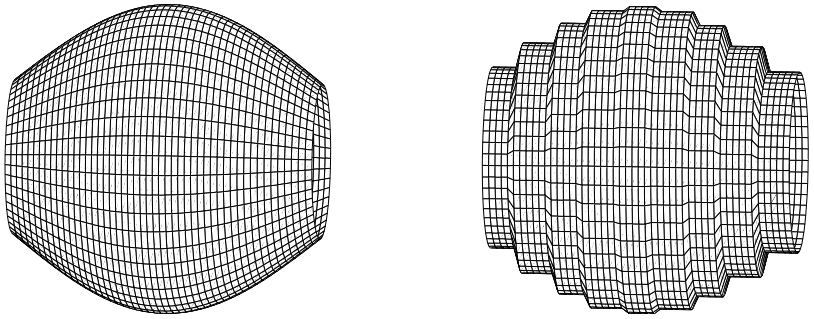

Figure 3.2: Comparison between the devised ideal soma (left) and the segmented implementation by NEURON (right).

328 μm, respectively) fall in the range of reported measurements
(306 ± 67.9 μm^2 [44]).

The neurons in nucleus laminaris are tonotopically organized: there is a high correlation between the neural position of the cell and the frequency to which the cell is tuned, termed the characteristic frequency (CF) of the cell. Thus, the position of the cell within the nucleus is a good predictor of the characteristic frequency of the cell [38], as defined in Eq. 3.3:

$$f = 40pos \tag{3.4}$$

where *pos* refers to the relative position (in percent) along the tonotopic axis, from the caudolateral (low frequencies) to the rostromedial end (high frequencies). Nucleus laminaris neurons are homogeneous in segregating their dendrites in a bipolar fashion: one tuft of dendrites extends dorsally and the other ventrally. Along the tonotopic axis, there is a gradient of decreasing length of the dendrites and increasing number of primary dendrites. Eqs. 3.5 and 3.6

characterize these relations as a function of the neural position of the cell [44]:

$$N_{den} = max(0.37pos - 5.5, 2) \tag{3.5}$$

$$L_{den} = \frac{(-11.19pos + 1447)}{max(0.37pos - 5.5, 2)} \tag{3.6}$$

where N_{den} is the number of primary dendrites, and L_{den}, the equivalent length of each dendrite, is the quotient between the total dendritic length and the number of primary dendrites.

The dendrites are modeled as unbranched cylinders in accordance to the simplified ball-and-stick model proposed by Rall (cf. Section 2.1). The dendrites are grouped around both ends of the major axis of the soma. Their section diameter is kept constant at 1.78 μm for all cells [44] and their length and number are computed as a function of the characteristic frequency of the cell. This relation is obtained by combining Eq. 3.4 into Eqs. 3.5 and 3.6; the result is plotted in Figure 3.3. Thus, the number of dendrites ranges tonotopically from 2 at CFs below 800 Hz to 14 at CF of 2 kHz. Similarly, the dendritic length varies from around 650 μm at CFs below 800 Hz down to 70 μm at CF of 2 kHz. The minimum number of primary dendrites is set to 2 to preserve symmetry (one on each side), which causes a minor artifact on the relation of the length of the dendrites as a function of the characteristic frequency of the cell.

Despite the outlined uniformity in the size of the soma and the reported constant diameter of the dendrites throughout the whole nucleus laminaris, there is some additional anatomical evidence that shows larger cells progressively tapering their diameter from the somatic region towards the dendrites. The implication of this phenomenon is a marked increase in the membrane surface, which in turn alters the total conductances of the cell and its behavior. Initially,

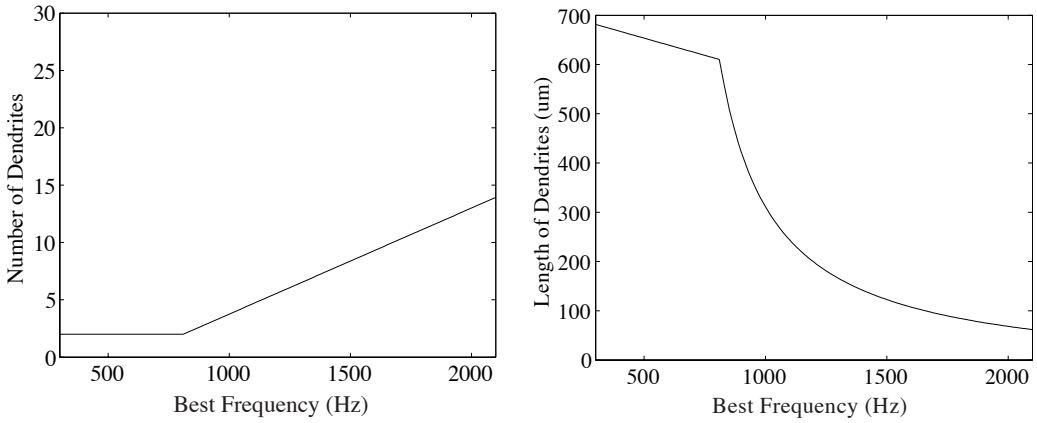

Figure 3.3: Number of primary dendrites and dendritic length as functions of characteristic frequency.

this effect is disregarded. It will be exhaustively analyzed in Section 5.3.

The axon of NL protrudes from the soma in between the two dendritic zones and initially extends medially for up to a few hundred micrometers [44]. The axon has an initial segment, also termed axon hillock, after which it becomes myelinated. The initial segment is reported to be 30 μm long and to have a mean diameter of 2 μm [2]. The diameter shows no variation between the axon hillock and the myelinated axon, and the internodal length of each myelinated segment is 60 μm (data from the barn owl) [2].

In the model, three different sections compose the axon: the axon hillock, the myelinated axon and the first node of Ranvier. All three sections are modeled as cylinders of constant diameter (2 μm). Whereas the axon usually projects to other parts of the brain several hundreds of micrometers away, the study of nucleus laminaris cells is limited to the first node of Ranvier, where the output of the cell is evaluated. In this study, the node is only regarded as a very small compartment where a spike is generated if the signal coming from the soma raises

above a certain threshold. Thus, the length of the node is set to 2 μm (data from the rat) [31]; the intended functionality compensates the lack of accuracy in the exact morphology of the node.

3.2 Electrical Properties

The membrane of the cell is mainly constituted of proteins and lipids. The latter form the basis of the membrane arranged in two parallel layers that isolate the intracellular cytoplasm from the extracellular medium. From an electrical point of view, the thin membrane acts like a capacitor. In membrane biophysics, the capacitance is usually characterized by the specific capacitance per unit area C_m, measured in microfarads per square centimeter (μF/cm^2). The generally agreed upon value for C_m is 1 μF/cm^2 [21]. Among the many kinds of proteins that populate the membrane, of special electrical relevance are those that enable ions to cross the membrane. The proteins that allow a current flow through the membrane are known as ion channels, and are modeled as resistors. The membrane resistance is usually specified in terms of the specific membrane resistance R_m, expressed in terms of resistance per unit area (Ωcm^2). Equally common is to express this same value in terms of the inverse of R_m, namely the specific leak conductance, $G_{leak} = 1/R_m$, measured in units of siemens per square centimeter (S/cm^2). The latter nomenclature is the one which is used in the model.

The cytoplasm of the cell is characterized in terms of the specific intracellular resistivity (R_i), defined as the total resistance across 1 centimeter cube of intracellular cytoplasm. The value conventionally used for R_i in avian and mammalian neurons is 200 Ωcm [21], which is set uniformly through all sections

of the model. Given a cylindrical axon or dendrite of diameter d and length L, its total resistance will be $4R_iL/\pi d^2$.

The simplest of all neuronal models characterizes the electrical properties of neurons with a resistance and a capacitance in parallel (the so-called RC circuit). This is the skeleton for each segment of every section modeled by NEURON. Adjacent segments are connected by means of a series resistance, and the dynamics of the voltage along segments are described by linear cable theory (for a review see [19, 21]).

All sections of the model share the same values for C_m and G_{leak}, except for the myelinated axon. The myelin membrane of an axon consists of several concentric wrappings of the axonal membrane. Its electrical properties can be obtained by adding together the contribution of each of its layers. The capacitance associated with one single layer of the membrane is:

$$C_{membrane} = C_m Area = C_m d\pi L \tag{3.7}$$

where one can use a planar approximation of the external surface of the cylinder because the width of the membrane is more than 100 times smaller than the axonal radius. For the myelinated case, the planar approximation does not hold anymore, and thus the associated capacitance should be calculated as (cf. Figure 3.4):

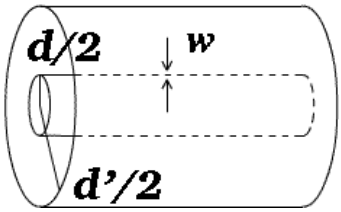

Figure 3.4: Dimensions of the equivalent cylinder.

$$C_{myelin} = \frac{C_m 2\pi w L}{ln(d'/d)} \tag{3.8}$$

Anatomical observations yield a relatively constant ratio d'/d of 0.7 throughout all the nervous system [26, 31], and a relatively constant width of the axonal membrane around 8 nm [26, 37]. Combining Eqs. 3.7 and 3.8, the ratio between the two cases can be expressed as follows:

$$\frac{C_{myelin}}{C_{membrane}} = \frac{2w}{dln(d'/d)} = \frac{1}{45} \tag{3.9}$$

which means that the myelination of the axon is equivalent to 45 wraps of one single membrane. Consequently, the equivalent capacitance for the myelinated section is the sum of 45 capacitors in series ($C_m/45$), and the resulting resistance is the sum of 45 resistors in series ($45R_m$). The lower capacitance and bigger membrane resistance result in an increased conduction velocity of the action potential through the fiber.

To get an estimate for the membrane resistance, one has to refer to physiological recordings. This value is obtained experimentally by injecting a series of current pulses into the cell, and measuring their voltage response. Using Ohm's Law, one can calculate the input resistance of the cell, namely the total membrane resistance. Current clamps should be recorded close below the resting potential to avoid the interfering effects of other conductances that become active at either more depolarized or more hyperpolarized voltages. For a set of cells with characteristic frequencies between 800 Hz and 3000 Hz [36], the mean input resistance (R_{in}) is measured to be 72 $\pm$ 34 MΩ. A 2000 Hz cell is chosen as the representative case from the mentioned set. To derive the specific membrane resistance, the input resistance must be multiplied by the total area of the cell:

$$R_m = R_{in}\ (Area_{soma} + Area_{den} + Area_{axon}) \tag{3.10}$$

$$G_{leak} = 1/R_m \tag{3.11}$$

which gives a result of G_{leak}=2.1E-04 S/cm^2. This value carries some degree of uncertainty for two reasons: the original measurement had a relative error (standard deviation) of about 50%, and this value is completely dependent on the area of the cell for which there is a large interval of incertitude.

The last element that remains to be characterized in order to describe the electrical properties of the passive membrane is a fictive battery V_{leak} that accounts for the resting potential. The value is obtained from a voltage-current plot of the experiment described above (cf. Figure 2E [1] in [36]). V_{leak} is the intersection of the slope below the resting potential with the abscissa I=0 nA, as if there were no other channels that actually shift this value towards more negative values. The intersection occurs at -50 mV.

The equivalent circuit of all elements of the passive membrane and the intracellular cytoplasm is depicted in Figure 3.5, as well as the evolution of the membrane potential when a current step of different amplitudes (-0.5, -0.1, 0.3, and 0.7 nA) is switched on at t=5 ms and turned off at 25 ms. Plotting the relation between this series of currents and voltages (in steady state) results in a linear regression of 72 MΩ, which shows self-consistency of the model.

3.3 Channel Dynamics

The hallmark of nucleus laminaris neurons, as part of the auditory system, is their ability to phase-lock and maintain high discharge rates. The next step in

[1] The plot is shifted -10 mV to match the resting potential (injected current of 0 nA) with the reported mean value in the same article: -59 ± 5 mV.

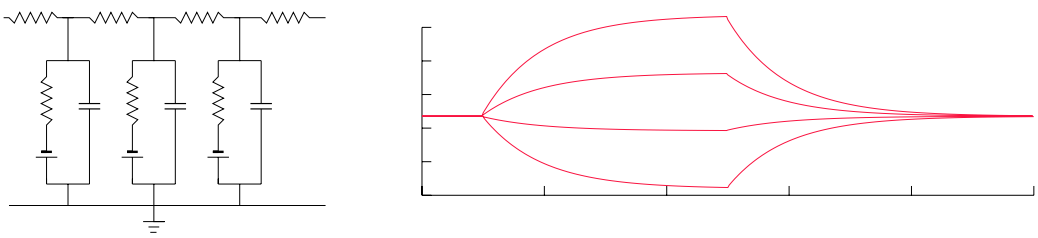

Figure 3.5: Equivalent circuit and behavior of the passive membrane.

the characterization of these time-coding neurons is to examine the mechanisms that can account for such precision. The primary source of explanation are the characteristic membrane properties of NL cells: voltage- and time-dependent ion channels that shape the action potential. In nucleus laminaris, two major ion conductances have been clearly identified: sodium (Na^+) and potassium (K^+). Additionally, two kinds of potassium permeabilities have also been differentiated. Based on an extensive set of experiments available in the literature that have tried to characterize their kinetics, voltage sensitivity and pharmacology, the classification of the three main types of ion channels present in nucleus laminaris is as follows:

Low Voltage Activated Potassium (K_{LVA}) This subtype of K^+ (Kv1 subfamily [4]) channel is responsible for the strong outward rectification near rest that auditory neurons exhibit: the voltage response to a depolarizing current step is substantially smaller than to an equivalent hyperpolarizing step [36]. The strong rectification compensates an excessive depolarization caused by high rates of input stimulation. Too much depolarization would inactivate the sodium conductance, preventing the cell from firing repeatedly and synchronizing to high frequencies. This channel, which is Dendrotoxin-I (DTX) and 4-aminopyridine (4-AP) sensitive [23],

presents rapid activation near rest (low threshold) and slow or partial deactivation.

High Voltage Activated Potassium (K_{HVA}) Belonging to the Kv3 subfamily of K^+ channels, K_{HVA} is characterized by positively shifted voltage dependencies and very fast deactivation rates [29, 40]. These properties allow this channel to enable fast repolarization of action potentials without compromising spike initiation or height, which maximize the quick recovery of resting conditions after an action potential. Narrowing the width of action potentials, K_{HVA} enables repetitive firing at high frequencies. Because of its high threshold of activation this channel is also known as delayed rectifier. It is tetraethylammonium (TEA) sensitive.

Sodium (Na) Not much is known about the intricacies of sodium dynamics due to its inherent faster kinetics, which pose greater difficulties in conducting the corresponding neurophysiological experiments. When the membrane potential reaches the firing threshold, the sodium channels boosts the membrane voltage to trigger an action potential, and repolarizes it to rest afterwards.

The Hodgkin and Huxley original study (cf. Section 2.2, [17]) of the ionic conductances underlying the action potential serves as the basic framework for modeling the ionic conductances in the model. The challenge resides in accommodating the abundant data from very diverse sources to conclusively depict the observed functionality of the neurons under study. Due to the limited number of neurophysiology experiments reported in nucleus laminaris [23, 36], most of the data comes from the previous nucleus in the auditory pathway that projects onto it, namely nucleus magnocellularis (NM) [22, 34, 35, 50].

Additional data is gathered from physiology and modeling in the medial superior olive (MSO) [45], the mammalian analog of NL. Data from the rat [25, 41] is also observed to characterize the sodium channel. Finally, previous models are taken either as a starting point [42] or as a partial reference [1, 6].

The first step in incorporating the sodium and potassium channels into the model is to try to quantify their presence in real cells. Membrane channels are expressed in the model in terms of concentrations per unit area. A procedure similar to the one explained to calculate G_{leak} (cf. Section 3.2) is used here to estimate both potassium conductances. Using data from a set of experiments in nucleus magnocellularis where the effects of K_{LVA} and K_{HVA} have been isolated and characterized independently, one can extract the associated total conductance for each channel: 0.1 μS and 0.45 μS, respectively (slope in current-voltage plot: Figures 5A and 7A in [34]). To express these magnitudes in terms of concentrations per unit area, the total membrane surface is computed through the measured capacitance [34]:

$$Area_{total} = \frac{C}{C_m} = \frac{14\ pF}{1\ \mu F/cm^2} = 1.4\text{E-}05\ cm^2 \tag{3.12}$$

$$G_{K_{LVA}} = \frac{0.1\ \mu S}{Area_{total}} = 7.1\text{E-}03\ S/cm^2 \tag{3.13}$$

$$G_{K_{HVA}} = \frac{0.45\ \mu S}{Area_{total}} = 3.4\text{E-}02\ S/cm^2 \tag{3.14}$$

It is important to note that neurons in NM tend to be bigger than their NL counterparts, and are usually spherical without any dendrites [39]. Therefore, the calculated channel densities refer only to the soma and the axon. However, without any other initial assumption, these densities are uniformly extended to the dendrites in the model, setting them equally across the soma, the axon hillock and dendrites.

No specific values for sodium densities have been found in the literature in any similar nucleus. To set the order of magnitude of this value, the channel density reported in the original Hodgkin and Huxley experiments in the squid giant axon (1.2E-01 S/cm^2 [17]) is used as a reference, because the corresponding densities for potassium and leak (3.6E-02 and 3.0E-04 S/cm^2) are in the same range of values as the ones in the model calculated previously (4.1E-02 and 2.1E-04 S/cm^2).

The reversal potentials for each of the channels are initially set accordingly to the values reported in the corresponding paper: E_K=-83 mV [34] and E_{Na}=40 mV [17]. The rest of parameters that determine the specific kinetics of each channel are summarized in Table 3.1. The parameter exponent refers to the power of each gating variable, namely the number of independent fictional gating variables that make first-order transitions between an open and a closed state (cf. Eqs. 2.10 and 2.11).

The protein channels that modulate the flux of ions through the membrane of the cell are temperature-sensitive. Thus, whenever a rate is given, it is accompanied by the specification of the temperature of the experiment (T_0). In biology, the effect of temperature (T) on rates is frequently given as the 10-degree temperature coefficient (Q_{10}) defined as rate(T+10 °C)/rate(T) [12]. In the model, the temperature for the simulations is set at 35 °C to reproduce the conditions of the cell *in vivo*. The temperature coefficient in the simulations is set by:

$$Q_{simulations} = (Q_{10})^{\frac{35-T_0}{10}} \tag{3.15}$$

where $Q_{simulations}$ multiplies the differential equation governing the kinetics of n for potassium (cf. Eq. 2.4), and the corresponding ones for m and h for sodium.

Thus, for a Q_{10} of 3 and temperature increases of 1, 5, 15 and 25 °C, the rates of gating increase are 1.12-, 1.7-, 5-, and 16-fold, respectively.

		K_{LVA}	K_{HVA}	Na	
		n	n	m	h
$\alpha_{V_{1/2}}$	(mV)	-60	-19	-40	-65
α_k	(mV)	21.8	9.1	10	20
α_0	(ms^{-1})	0.2	0.11	4	0.07
$\beta_{V_{1/2}}$	(mV)	-60	-19	-65	-35
β_k	(mV)	14	20	18	10
β_0	(ms^{-1})	0.17	0.103	4	1
exponent		1	1	3	1
Q_{10}		2	2	3	
T_0	(°C)	23	23	6.3	

Table 3.1: Parametrization of channel kinetics.

Chapter 4

Physiological characterization

Once the model has been built with all the parameters set matching the values reported in the literature, the model should be expected to behave like real cells. However, due to the variety of sources employed, the resulting initial set of parameters does not match the cell's behavior reported in any of the sources (as an illustrative example, cf. Figure 4.1). Many simulations have to be run to progressively assess the importance, the degree of variability and reliability of each choice of values for a given parameter space.

The large extent of the initial parameter space makes it impossible to address the characterization of all different variables involved at once. Thus, the tuning of the parameters is done in consecutive stages following the guidelines set up by the reports found in the literature. Diverse physiological experiments try to characterize each aspect of the functionality of the cell as separately as possible, and they are reproduced up to a reasonable extent in the model in order to attain the characteristic behavior of nucleus laminaris cells as coincidence detectors.

4.1 Subthreshold response

The first feature to be studied in detail in nucleus laminaris neurons is their outward rectification. Physiological experiments characterize the subthreshold response of the cell by injecting a series of current steps of different amplitudes and recording the voltage response at its steady state. The rectification is clearly visible by plotting the relation between the injected current (I) and the membrane voltage (V) in an V-I plot. These experiments are mimicked in the model, where the hypothesis is made that K_{HVA} and Na do not have any influence on rectification, and they are therefore temporarily removed. The hypothesis is based on two assumptions. Firstly, K_{HVA} channels become active at much more positive values, and they should be inactive at the range of voltages under study. Secondly, although some current injections may indeed depolarize the membrane voltage above the voltage threshold triggering a spike at the very beginning of the step, sodium channels quickly inactivate and the membrane voltage stabilizes at the rectified value. The correctness of the hypothesis is tested once the channels have been faithfully characterized.

The reference is taken from the V-I plot pictured in Figure 2E in [36], although the whole figure is shifted by -10 mV so that the resting potential matches the mean value reported in the same paper (V_{rest}=-59±5 mV). The first simulations run with the parameters set at their initial values (cf. Chapter 3), show two main differences with the reference plot: V_{rest}=-77 mV and rectification occuring at much more hyperpolarized values (cf. Figure 4.1).

The first thing to be considered is that the midpoints for activation and deactivation of K_{LVA} have been taken from nucleus magnocellularis in absolute terms, but they should be considered relative to the cell's resting potential

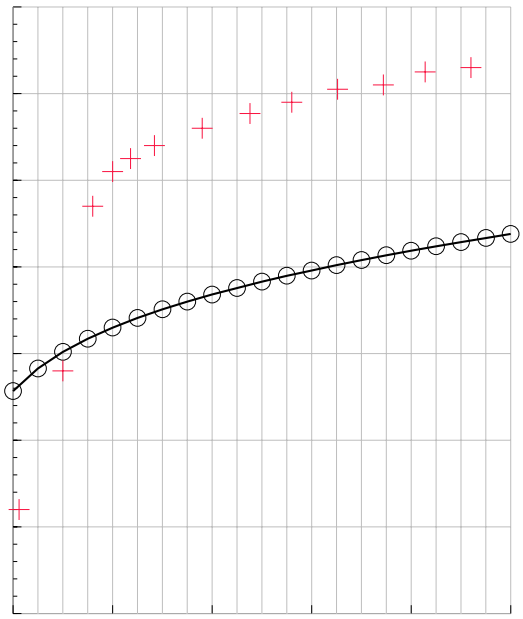

Figure 4.1: Comparison between the V-I plot for the initial set of parameters (black circles) and the reference curve (red crosses, Figure 2E in [36] shifted -10 mV).

(reported to be -66±7 mV [34]). The resting potential results from the equilibrium of intracellular and extracellular concentrations of all ions that can flow through the membrane, and thus there is a reciprocal dependence between the channel dynamics and the value where V_{rest} is.

The second observation refers to the calculated conductance associated with K_{LVA} channels. The total conductance was measured for nucleus magnocellularis cells and divided by their mean area (cf. Eqs. 3.12 and 3.13). The channel density was exported to NL, assuming the same channel density for both types of cells. However, due to the larger area in NL cells because of their dendrites, the total conductance is much bigger, which results in greater rectification. Instead,

if the value exported is the total conductance, and it is later divided by NL cells' mean area, the total conductance is similar, and so is the cell's behavior.

A preliminary exploration of the parameter space around the initial values for the variables governing the K_{LVA} channel kinetics and K_{LVA} densities revealed that a good fit to the reference plot was hard to find. The reference plot did not seem to be a good representative for the general case. Accordingly, the reference was adapted to the mean values reported in the text of the paper, whose main features are: V_{rest}=-59±5 mV, slope resistance below resting potential at 72±34 MΩ and slope above resting potential at 11±8 MΩ. To quantify the degree of similarity between the outcome of the model and the reference plot, the mean square error was computed for each of the constraints weighted against the reference values as follows:

$$Error = \left(\frac{slope_{below\ rest} - 72}{10}\right)^2 + \left(\frac{slope_{above\ rest} - 11}{2}\right)^2 + \left(\frac{V_{rest} + 59}{2}\right)^2 \quad (4.1)$$

Comparing the V-I plots for NM and NL (Figure 1B in [34] or Figure 4B in [49] and Figure 2E in [36]), one can observe that rectification is more abrupt in NL. Thus, faster and stronger rectification can be obtained by simultaneously decreasing the channel density and reducing the range in which K_{LVA} becomes active (making α_{nk} and β_{nk} smaller).

There are more parameters to specify the dynamics of K_{LVA} than constraints available from biological data. Therefore, no ideal solution exists for this set of parameters, except that they provide with reasonable behavior for the cell. A few guidelines about the parameters governing the dynamics of K_{LVA} can be outlined as follows: the midpoints for activation and deactivation ($\alpha_{nV_{1/2}}$ and $\beta_{nV_{1/2}}$) are

between 10 and 15 mV above rest; the activation and deactivation ranges α_{nk} and β_{nk} tend to be inversely proportional to the difference between V_{rest} and $\alpha_{nV_{1/2}}$ or $\beta_{nV_{1/2}}$; the bigger the activation and deactivation ranges, the smaller (i.e. faster) the activation and deactivation rates (α_{n0} and β_{n0}). Such relations between K_{LVA} parameters define a relatively small valid variable space. Three different sets of parameters that give a valid voltage-current relation are summarized in Table 4.1 and depicted in Figure 4.2: red traces mark the reference, and blue traces plot the slopes where the mean square error is computed below and above rest.

		Set 1	Set 2	Set 3
$\alpha_{V_{1/2}}$	(mV)	-50	-50	-45
α_k	(mV)	5	10	8
α_0	(ms^{-1})	0.20	0.05	0.20
$\beta_{V_{1/2}}$	(mV)	-50	-50	-45
β_k	(mV)	5	10	8
β_0	(ms^{-1})	0.17	0.10	0.17
$\overline{G_{K_{LVA}}}$	(S/cm^2)	0.0015	0.0035	0.004

Table 4.1: Three different sets of parameters for K_{LVA} that give a valid voltage-current relation.

4.2 Stimulus-evoked postsynaptic potentials

The ultimate goal of this study is to examine the responses of NL neurons to stimuli that closely resemble acoustic stimuli. Nucleus laminaris receives its inputs from nucleus magnocellularis axons projecting onto NL dendrites. *In vivo*

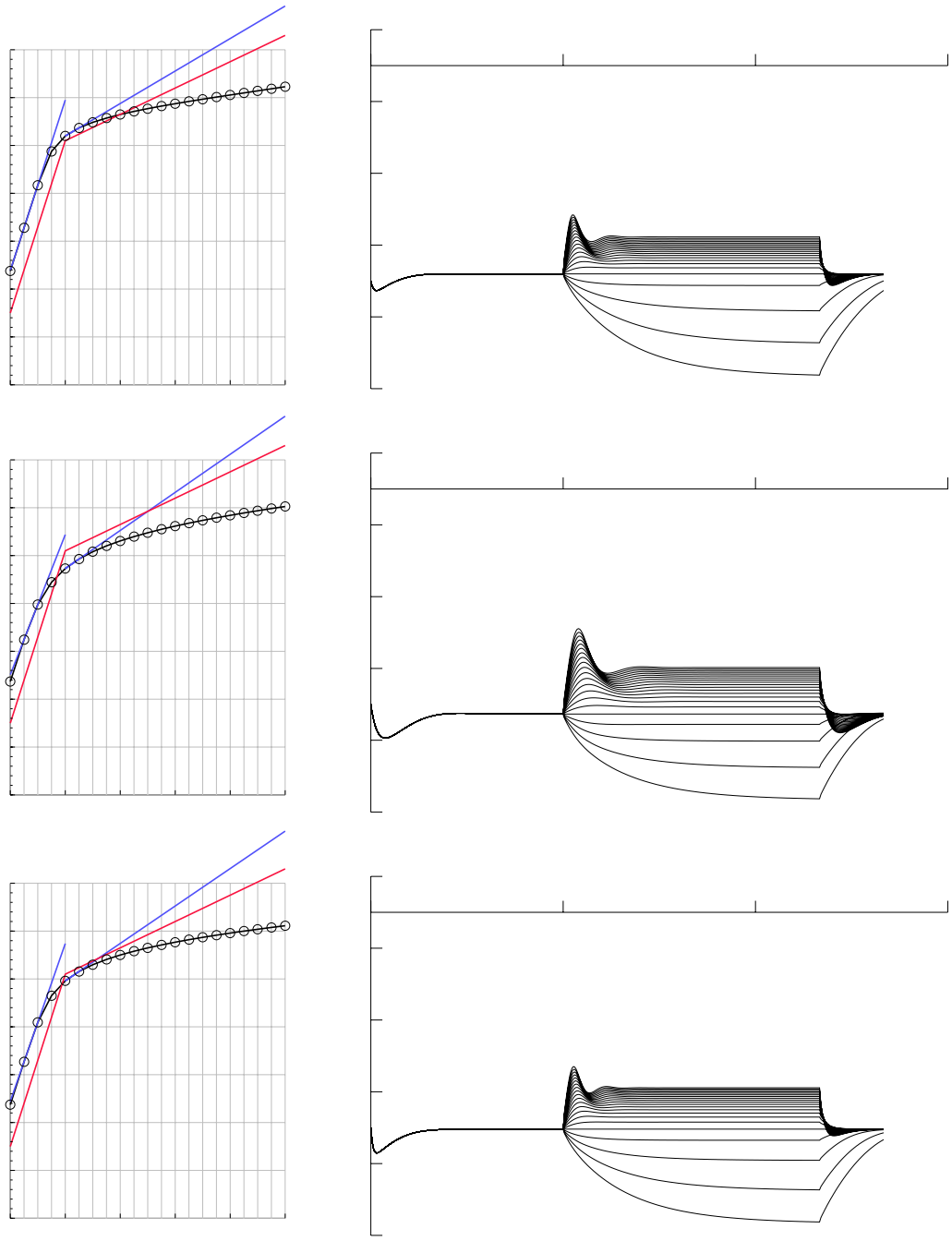

Figure 4.2: Valid voltage-current curves and their correspoding time plots.

recordings reveal that NM fire action potentials phase locked to acoustic stimuli and that the average firing rate (AFR) of NM neurons does not vary systematically with their characteristic frequencies [3, 47]. Accordingly, in the model, AFR is set fixed at 250 Hz [36] and does not vary with the stimulus frequency.

In order to replicate the postsynaptic potentials (PSPs) elicited by nucleus magnocellularis, the next step is to model the shape and size of the unitary PSPs. Postsynaptic potentials are described by a change in the membrane voltage shaped by an alpha function of the form:

$$G_{syn}(t) = \frac{\overline{G_{syn}}t}{\tau} e^{(1-\frac{t}{\tau})} \tag{4.2}$$

$$I_{syn} = G_{syn}(V - V_{syn}) \tag{4.3}$$

where $\overline{G_{syn}}$ is the amplitude of the PSP, τ determines the shape, t is time, and V_{syn} is the reversal potential for the synaptic current that is set to 0 mV according to the referred paper. $\overline{G_{syn}}$ is set to 7 nS so that the evoked PSPs have a mean amplitude around 1.5 mV (Figure 3B [36]). The reported half-width of the alpha function is 0.76±0.50 ms; a τ of 0.33 ms is proposed in that study to match their measurements. However, a straightforward computation of such a function gives an ideal half-width of 0.89 ms. Additionally, the plasma membrane adds a low pass filter effect (RC circuit) that widens the response. Due to the physical impossibility of implementing the suggested value, a value of 0.1 ms is chosen for τ, which results in a half-width of around 1.2 ms. It is relevant to mention that other experiments report postsynaptic potentials with much slower time constants: half-widths between 2.2±0.4 ms and 5.4±0.5 ms depending on the age of the chick (post-hatch days (P) 2-7 and embryonic days (E) 16 and 17,

respectively) [23]. The reference experiments were made with embryos E19-21 [36].

In the simulations, the size of PSPs are adjusted by varying the injected current given by Eq. 4.3 while the cell membrane potential is at rest, mimicking the physiological experiments. These measurements give an estimate on how fast the membrane can respond to a given stimulus. The speed of the membrane is directly related to the total membrane conductance at a given time. Because K_{LVA} starts becoming active near rest, these measurements are a good estimate on how much K_{LVA} conductance is active above the resting potential, as the leak conductance by itself cannot account for such a fast response. In the previous section, the reference for matching K_{LVA} conductances was taken just above rest to ensure a sufficient amount of conductance at this point for the membrane to follow the synaptic stimuli.

4.3 Suprathreshold response

The hallmark of nucleus laminaris neurons is their ability to fire action potentials phase locked to the incoming stimuli. Despite being the main agents in shaping the action potential, sodium currents are less well known due to the fact that they are large and fast, which makes them hard to voltage clamp without introducing artifacts. The most arduous task in constructing the model is probably the accurate characterization of the kinetics of sodium channels.

The axon hillock is believed to be the site for spike initiation, from where the action potential propagates forward through the axon and backwards to the soma. High density of Na in the initial segment compared to the soma accounts for this phenomenon. Although there is increasing evidence for the presence of

sodium in the dendrites, it is speculated to be of another type [7]. Electrophysiological studies have differentiated between a fast or transient Na^+ current and a persistent Na^+ current. The transient current mediates the fast action potential, while the persistent current activates below threshold and is thought to help boost currents in the dendrites. However, the magnitude of the persistent Na^+ current is approximately 1% of the transient one (for a review, see [7]). In order to maintain simplicity in the model, only one type of sodium channels (transient) has been incorporated, and the channel densities of the soma are a fraction (1/3) of these present in the axon.

The first adjustment to the initial set of sodium parameters is a shift in the reference temperature T_0 from 6.3 to 23 °C. The motivation for this change is to bring some internal coherence to the model, so that all three channels included therein have the same reference temperature, and they can be directly compared if necessary. Additionally, 23 °C is the temperature of most *in vitro* experiments in avian and mammalian nerve cells, and it is the reference for most of the data from the literature. Q_{10} is shifted from 3 to 2, accordingly. This first modification will make the original specifications for sodium much slower at the simulation temperature (35 °C) because the differential equation that governs the sodium kinetics is now multiplied by a smaller factor (cf. Eq. 3.15).

Without any further modifications, some preliminary simulations are run to gain some intuition about the changes to be made. The results show that the cell cannot fire even a single action potential, and the resting potential is critically shifted towards more positive values (cf. Figure 4.3, upper plot). Two straightforward explanations can account for the observed disparities. Firstly, the original values are referenced to a resting potential of -65 mV instead of -59 mV,

which causes a similar misbehavior as observed in the K_{LVA} case (cf. Section 4.1). Secondly, the sodium channels were originally tied to some other potassium ones that had an activation range (α_{nk}) of 10 mV, which now has been reduced in K_{LVA} to 5 mV (Set 1), which makes potassium stronger in the zone where it becomes active, shutting down a weaker sodium. To illustrate these two arguments, if all activation and inactivation ranges are halved for sodium and their midpoints of activation and inactivation are shifted at least +6 mV, some spiking starts to occur (cf. Figure 4.3, middle plot). However, some undesired oscillation occurs after the initial spike resulting from breaking the fragile equilibrium between both channels. In order to fix these undesired effects, a more careful treatment of the channel kinetics is required.

In order to acquire a complete picture of the mechanisms involved in shaping the action potential, K_{HVA} must also be taken into consideration. Unlike K_{LVA}, K_{HVA} cannot be depicted isolated because it interacts with Na in the same voltage range near the peak of the spike. Without any additional information from the original specifications for K_{HVA}, the channel is incorporated in the simulations. However, after having changed K_{LVA} densities (cf. Section 4.1), the channel densities are readjusted to meet the original proportions (82% of K_{HVA} versus 18% of K_{LVA}) as reported in the reference [34].

The complexity in adjusting the parameters for the sodium channels comes from the two imaginary gating variables needed to account for the involved dynamics observed in physiological experiments, instead of the single one in the potassium case. Twice as many parameters have a devastating effect in trying all possible combinations, which increase exponentially with the number of variables.

The main concern in finding an appropriate set of sodium parameters is to

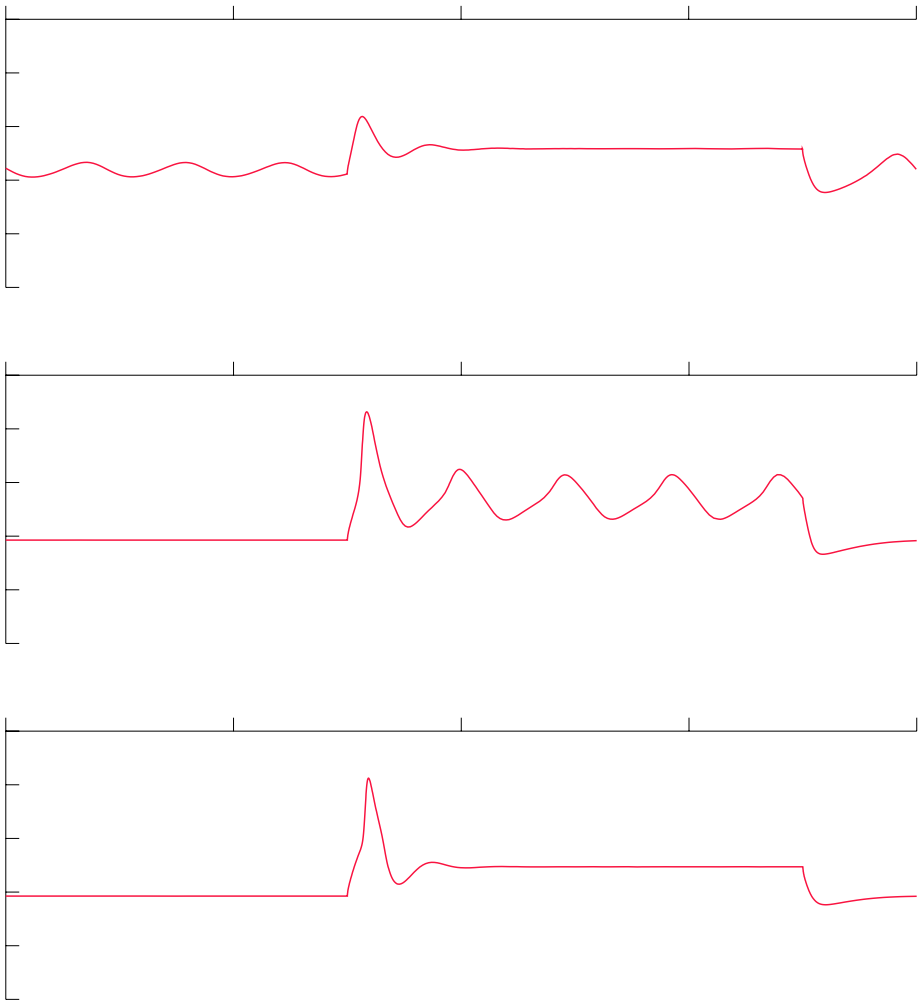

Figure 4.3: Membrane voltage response to a 2 nA current clamp injected in the soma using the specifications for K_{LVA} of Set 1 and $\overline{G_{Na}} = 0.05$ (axon hillock) . The upper graph shows the response for the initial configuration of Na channels (Hodgkin and Huxley [17]). The middle graph plots the response after shifting $\alpha_{mV_{1/2}}$, $\beta_{mV_{1/2}}$, $\alpha_{hV_{1/2}}$ and $\beta_{hV_{1/2}}$ by +6 mV and dividing α_{mk}, β_{mk}, α_{hk} and β_{hk} by 2. The lower trace plots one of the multiple outcomes of the distributed simulations that matches the specifications imposed on the shape of the spike.

constrain the limits of the space to be searched. There are many examples in the literature that have characterized the sodium kinetics, either by means of physiological experiments alone, or combining them with computational models [5, 8, 17, 24, 25, 32, 41, 45, 46, 48]. Despite having the commonality of using a Hodgkin and Huxley typification of the channels described, some differ in the exact formulation of the equations. Nonetheless, there is an overlap in the range of valid variables between these models (it is important to reminder that ultimately they are describing the same physical phenomenon). The biophysical meaningful range is summarized in Table 4.2, and it has been corroborated in the model by manually running several test simulations.

		m	h
$\alpha_{V_{1/2}}$	(mV)	[-30,-50]	[-20,-60]
α_k	(mV)	[3,10]	[10,20]
α_0	(ms^{-1})	[0.5,5]	[0.05,0.15]
$\beta_{V_{1/2}}$	(mV)	[0,-60]	[0,-60]
β_k	(mV)	[5,20]	[5,10]
β_0	(ms^{-1})	[1,4]	[1,4]
$\overline{G_{Na}}$	(S/cm^2)	[0.03,2.0]	

Table 4.2: Biophysically relevant range of sodium parameters.

Having defined the starting point for the given variable space, all that remains is to specify the required outcome of the model. Mimicking the physiological experiments once again, a set of current clamps of different amplitudes are applied to the cell, and the action potential that the cell might or might not fire in response is evaluated as follows:

- Current clamp of 0.50 nA: no action potential is expected. The amount of injected current should not be enough to depolarize the cell up to the firing threshold (-42±6 mV [36]). The detection threshold is set at -40 mV, and if the membrane voltage of any cell crosses the threshold at this stage, the combination of parameters that define the sodium kinetics for this cell are discarded.

- Current clamp of 1.25 nA: the cell might or might not fire, but if it does, it can only fire once. The injected current brings the plasma membrane near the firing threshold. It is equally possible that there is enough current to activate the sodium channels or that they remain inactive. However, if one spike is triggered, the membrane voltage should repolarize to the clamped value afterwards without oscillating. The detection threshold is set at -40 mV, and it should be crossed at most once.

- Current clamp of 2.00 nA: the cell must fire one single action potential. The injected current has to depolarize the cell enough to activate the sodium channels, the cell must fire in response, and the voltage must repolarize to rest afterwards without oscillating. Two detection thresholds are set at -25 mV and -40 mV, each of which must be crossed only once. The first one is to ensure a minimum height of the spike (reported action potential peak of -15±17 mV [36]), and the second one is to detect lower second spikes. If the spike is not high enough or secondary spikes are detected, the associated combination of sodium parameters is discarded.

Current clamps are applied with a 25 ms delay after the simulation starts so as to be able to detect unwanted combinations of sodium parameters that make the cell spike at rest. The duration of the current clamp is set to 15 ms to be able

to detect oscillations when the membrane voltage repolarizes to the clamped value. According to the specifications of the biophysically relevant ranges summarized in Table 4.2, a set of representative values are chosen to explore the appropriate variable space for sodium parameters as detailed in Table 4.3. The total number of combinations to be simulated is 20480, which takes somewhat less than seven hours in 17 machines, with an average of 4 simultaneous simulations per machine.

		m				h			
$\alpha_{V_{1/2}}$	(mV)	-35	-40	-45	-50	-55	-65		
α_k	(mV)	5	10			10	20		
α_0	(ms^{-1})	2	4			0.05	0.1		
$\beta_{V_{1/2}}$	(mV)	-40	-45			-15	-20	-25	-30
β_k	(mV)	5	10			5	10		
β_0	(ms^{-1})	2	4			2	4		

Table 4.3: Simulated set of values for sodium parameters.

For the three sets of parameters that defined a reasonable V-I curve outlined in Section 4.1, these combinations are tried with two different values for the sodium conductance in the axon hillock ($\overline{G_{Na}}$=0.05 and 0.1 S/cm^2). In order to provide a notion of the number of combinations that matched the specifications, the outcome of the search for each set of parameters is summarized in Table 4.4. One of the multiple combinations obtained is plotted in Figure 4.3, lower graph.

	Set 1		Set 2		Set 3	
	Set 1a	Set 1b	Set 2a	Set 2b	Set 3a	Set 3b
$\overline{G_{Na}}$ (S/cm^2)	0.05	0.1	0.05	0.1	0.05	0.1
Number of combinations	5530	6988	9414	9829	3570	6010

Table 4.4: Outcome of the search for sodium parameters.

4.4 Firing rates

Gathering together the data obtained in the previous two sections, the next step in constructing a biophysically realistic model of nucleus laminaris is to evaluate the ability of the cell to respond to stimuli that closely resemble acoustic stimuli. The aim of the present section is to measure the relation between the stimulus frequency and the corresponding evoked firing rate of the cell, evaluating the phase locking capabilities of NL cells. The reference is taken from a set of physiological experiments where stimulus of different frequencies were applied directly to the somatic area of high frequency cells while varying the number of simulated inputs (Figure 4A in [36]).

The ability of the cell to phase lock to its synaptic inputs is closely tied to the dynamics of the sodium channels. Thus, the specifications for sodium channels are not yet complete. The requirement of firing an action potential at the onset of a current clamp does not guarantee the phase locking properties observed *in vitro* in nucleus laminaris cells. Figure 4.4 illustrate two combinations that matched the specifications for the shape of the action potential in the preceding section (two of the multiple combinations summarized in Table 4.4), but do not behave as expected in terms of their firing rates. Physiological experiments report that during 500 Hz stimulation the firing rate plateaus near 500 Hz. From

this maximum, the average firing rate decreases with increasing stimulus frequency. The left graph in Figure 4.4 plots a combination of parameters that is unable to phase lock no matter how many inputs are applied onto the soma, while the right plot depicts a combination that seems to plateau below 500 Hz, but shows an even higher firing rate for the 750 Hz stimulus case.

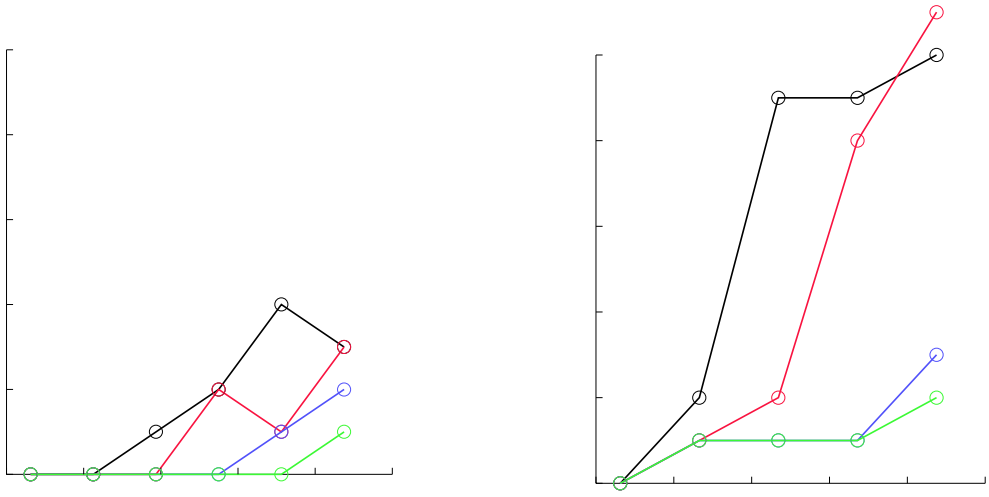

Figure 4.4: Two examples of unacceptable firing rate plots.

The computational cost of generating a firing rate plot, like the ones depicted in Figure 4.4, for every set of combinations found in the previous section is very high. Instead, specific points of the plot are chosen as a criterion to match the whole graph, through which all the combinations will be filtered. The reasons for chosing these particular points and not others rely on the intuition acquired running many simulations manually over the past months. However, the correctness of such a selection is the validity of the outcomes that result from the described process.

The first restriction is to impose a minimum and a maximum for the firing

rate of the cell in response to 750 Hz stimuli. The firing rate should be above 100 Hz and below 500 Hz when applying 70 simulated inputs onto the soma. On the initial phase of the present search, the constraints should not be too restrictive to avoid getting the empty set as the outcome of the filtering, but yet they have to make a selection on the existing sets. Despite the fact that the constraint might seem not very restraining, the result is a reduction in the number of combinations of about one fifth.

The second restriction is imposed on the 500 Hz stimulus case. For explanatory purposes, the search has been progressively constrained in consecutive phases. The first step forces a 500 Hz firing rate with 70 simulated synapses onto the somatic region, which is quite far from the minimum 30 synapses simulated in the reference paper. The same constraint is then imposed with 56 and 42 synapses. The number of synapses is a multiple of the number of dendrites (14) for simplicity resulting from the actual implementation of the model. The progression in the number of valid combinations is shown in Table 4.5.

Two of the outcomes of this search are plotted in Figure 4.5, where the left plot belongs to Set 1b and the right one to Set 3b. Not only do the firing rates plots match the reference, but the time plots of the voltage response are also similar to the ones recorded from physiological experiments. The divergence in the firing rates at every frequency from the local maximum or the steady state is also reported in the referred experiments, where *data points extending past the asymptotic region of the curves were not analyzed because large fluctuations often obscured action potentials* [36].

The last thing that remains to be done before completing the physiological

Criterion	Set 1a	Set1b	Set 2a	Set 2b	Set 3a	Set 3b
From previous section	5530	6988	9414	9829	3570	6010
AFR of 750 Hz with 70 synapses	332	1276	1115	3066	339	1368
AFR of 500 Hz with 70 synapses	131	805	336	2018	336	1337
AFR of 500 Hz with 54 synapses	20	360	25	377	202	1068
AFR of 500 Hz with 42 synapses	0	5	0	0	8	37

Table 4.5: Progression in the number of combinations that match successive constraints on firing rates.

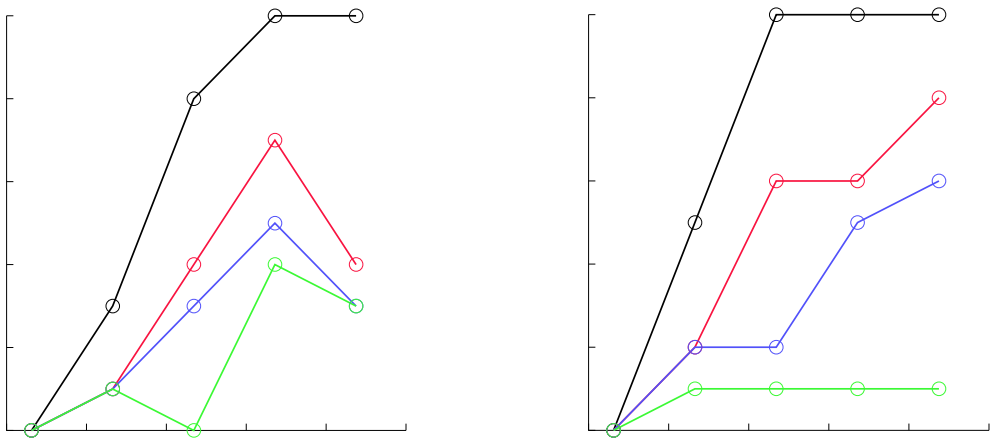

Figure 4.5: Two combinations with valid firing rates. Left graph belongs to Set 1a, and right graph belongs to Set 3b.

characterization of the high frequency cell under study is to corroborate the hypothesis formulated at the begining of the chapter. For simplicity, K_{HVA} and Na had been temporarily removed when characterizing K_{LVA}, arguing that they do not have any influence in the membrane voltage near rest. In some cases, K_{HVA} and Na introduce less than a 5% variation in the values used to test the validity of the corresponding V-I curves. A difference of 5% is less than the variability reported in physiological experiments, and it is thus perfectly acceptable. However, there are some other cases in which the presence of K_{HVA} and Na disrupts the resulting voltage-current relation. If that is the case, these combinations are consequently discarded because they do not match the specifications anymore. Table 4.6 shows the number of combinations that result from checking the voltage-current relation after completion, and Figure 4.6 depicts both a valid and a non-valid voltage-current relation taken from Set 3b.

	Set 1a	Set1b	Set 2a	Set 2b	Set 3a	Set 3b
Number of combinations	0	5	0	0	1	22

Table 4.6: Number of combinations matching V-I specifications with K_{HVA} and Na.

Analyzing the results obtained, no pattern on how the variable space evolves through the different stages of the search becomes evident. The higher number of combinations that match the different phases of the search oscillate between different stages, which makes the search especially difficult. Set 1 has given the best match in the voltage-current relation, but only results in 5 combinations matching the firing rates specifications. On the other hand, Set 2 gave the higher number of combinations for the shape of the action potential, but none of them

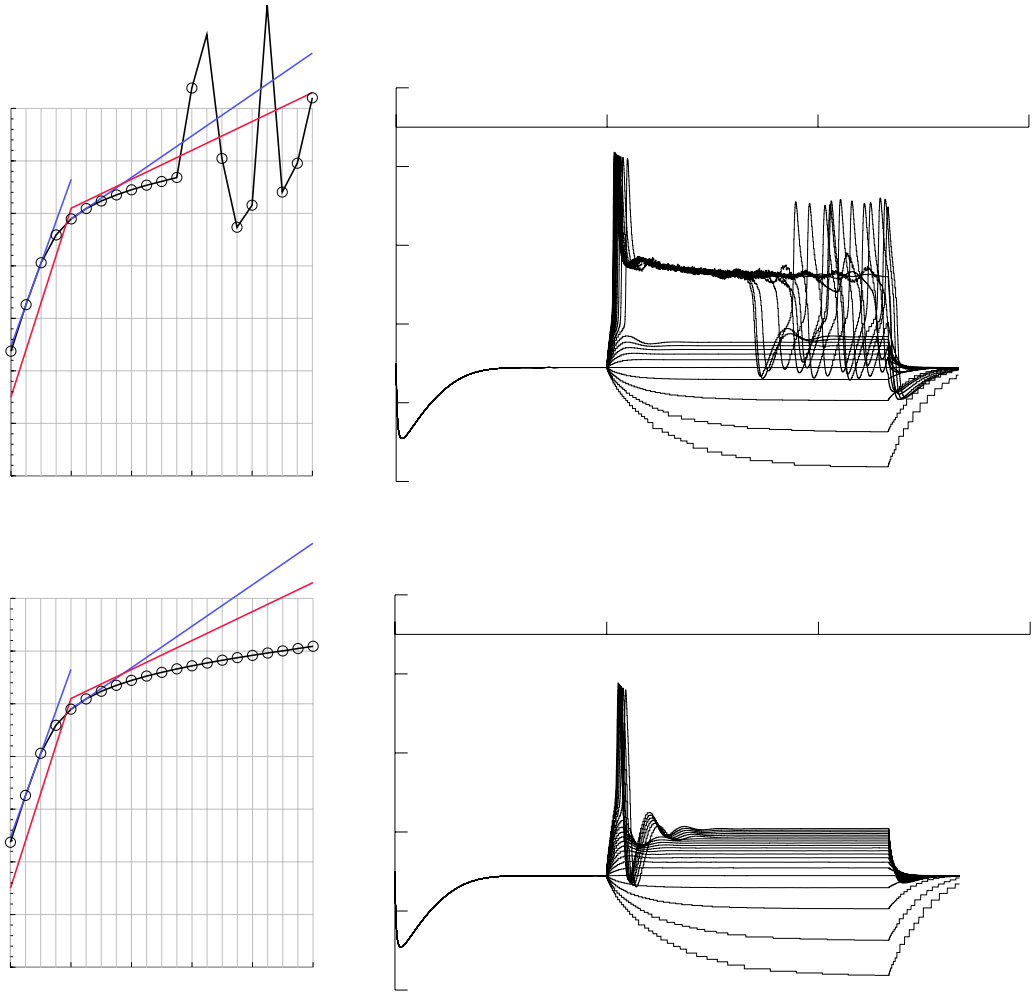

Figure 4.6: Invalid (top) and valid (bottom) V-I plot with K_{HVA} and Na.

matches the constraints imposed on the average firing rates. Somewhat in the middle of the first two, Set 3 gives the overall better results. The progression of the variable space shows that the difficulty in doing the search lies in imposing the appropriate degree of restriction, which can also be thought in terms of accuracy, at every stage. The appropriateness in the successive restrictions is only guided by intuition, which in turn is gained by experience. Nonetheless, the success of the search heavily relies on the computational power managed through the distributed simulations. The wise combination of both tools, biological intuition and computational power, in the extensive search of the parameter space is what ultimately ensures a successful outcome.

Chapter 5

Adjusting Tonotopicity

An average high frequency cell (CF=2000 Hz) has been chosen as the reference for characterizing nucleus laminaris behavior. The choice comes from the fact that most of the physiological recordings are conducted in the high frequency region of NL. However, a single cell cannot account for the variety of cells' performance observed throughout the nucleus. The first reported differences between cells in nucleus laminaris refer to anatomical variations along the tonotopic axis of NL (cf. Section 3.1). Physiological experiments also report divergent functionalities between cells located in different sites of NL. In order to analyze the implications of such variations, a second reference cell is chosen close to the other end of the tonotopic axis with a characteristic frequency of 500 Hz. The implicit framework of the present chapter is the gradient in the number of dendrites and dendritic length observed in NL cells [44].

5.1 Preliminary analysis

The 500 Hz cell has 2 dendrites of about 650 μm long, as opposed to the 2000 Hz cell that has 14 dendrites of 68 μm. The associated dendritic area for the two

cases is 4103 and 2990 μm^2, respectively. The first impression is that the larger dendritic area would result in bigger total conductances, which would mean smaller input resistances and faster time constants ($\tau = RC$). The implication is that the low frequency cells that compute slower time signals should be faster than the high frequency ones, which contradicts the observations from physiological experiments.

The first concept to bear in mind to understand this contradiction comes from the constraint imposed by the cable equation on the voltage along the cable: the stationary voltage distribution decays exponentially away from the site of injection. Therefore, the current will not flow through the membrane uniformly along the cable. In fact, it will only flow through the nearest portion of the membrane to the site of injection. The parameter controlling the decay is the space constant λ:

$$\lambda = \sqrt{\frac{R_m}{R_i}\frac{d}{4}} \tag{5.1}$$

The voltage decreases to e^{-1} (37% of its original value) at a distance λ from the site of injection, and to e^{-2} (13%) at 2λ. Different λs can be associated to the different conductances, namely leak and K_{LVA}, using the associated membrane resistances for each case (R_m). For the corresponding values reported in Section 4.1, λ_{leak}=325 μm and $\lambda_{K_{LVA}}$=121 μm.

It is clearly seen that in the high frequency cells the voltage flows through most of the dendritic length, whereas in the low frequency cells the 'effective' dendritic membrane is much smaller. Thus, the effective conductance is smaller for the low frequency cells, which makes them slower compared to high frequency cells.

Not only do the lengths of the dendrites make a difference in the behavior of

the cell, but the number of dendrites also influences its functionality. In order to analyze the effect of varying the number of dendrites, the equivalent circuit of the passive neuronal fiber (cf. Figure 2.2) is reconsidered; for simplicity the analysis is limited to the leak conductance, although it is straightforward to extend its implications to K_{LVA}. Figure 5.1 shows a simplified circuit, where each section has only one compartment, of a soma and two dendrites (left), and its equivalent circuit with one single dendrite.

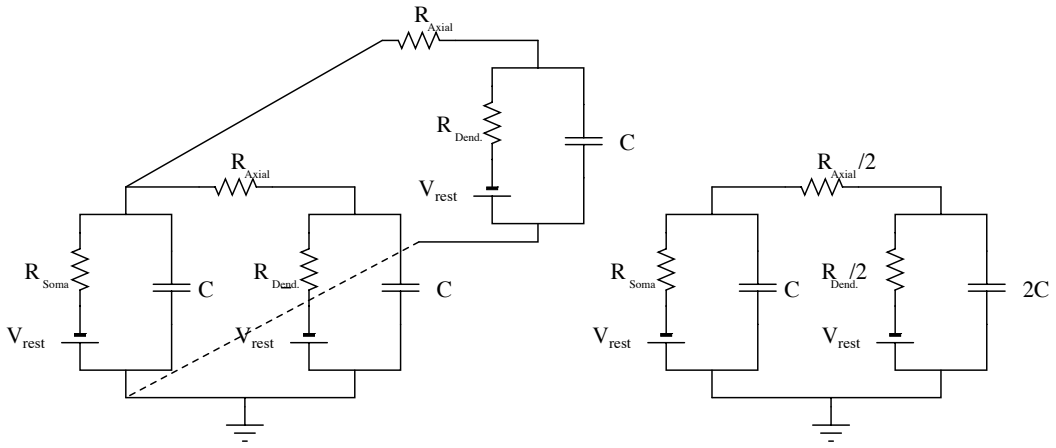

Figure 5.1: Simplified circuit of a soma and two dendrites, and its equivalent with only one dendrite.

In the general case, adding n dendrites of the same length results in dividing by n both the equivalent membrane resistance and the axonal resistance, as well as multiplying by n the equivalent capacitance. In electrical terms, the result is a greater coupling between the soma and the dendrites. The current injected in the soma will encounter less resistance to flow through the dendrites and consequently less current will flow through the somatic membrane, effectively slowing down the somatic membrane time constant. This effect makes cells with many dendrites (high frequencies) slower than those with fewer dendrites, which

is counterintuitive.

In order to evaluate which of the two factors has a predominant effect on the cell response, an initial simulation is run for the 500 Hz cell with the specifications for the channel kinetics and densities from the high frequency counterpart (Set 1b). Figure 5.2 shows the voltage-current relation and the corresponding time plots.

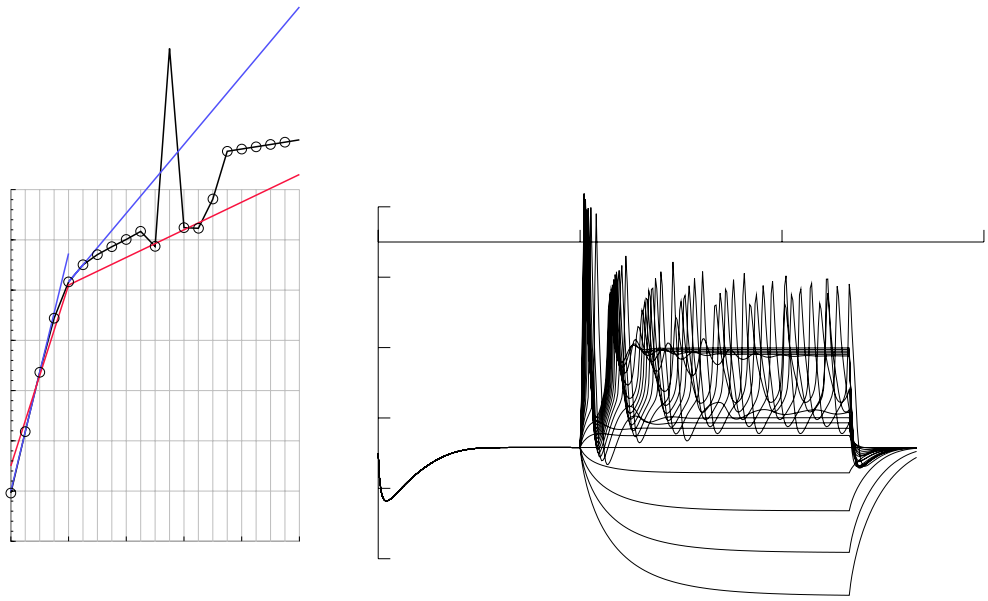

Figure 5.2: V-I plot for the 500 Hz cell with the configuration from the 2000 Hz cell.

The slopes above and below rest show bigger resistances (smaller conductances), that imply less rectification and slower time constants. The weaker rectification results in less amount of sodium to repolarize the membrane voltage after the peak of the spike, breaking the potassium dominance over sodium and causing oscillations after the initial action potential. However, in this case larger resistances do not cause slower time constants, because the decoupling

effect of the dendrites from the soma is stronger, which makes the cell faster (the time-to-peak is shorter for the low frequency cells compared to the high frequency ones).

To sum up, the fact that the low frequency cells are faster than the high frequency ones does not match the observations from physiology, and some modifications are needed to adjust the model to experimental data.

5.2 Redistribution of conductances

The first proposed modification to reconfigure the model is to change the distribution of the conductances between the soma and the dendrites, as done elsewhere in the literature [6]. The purpose is to make both cells (500 Hz and 2000 Hz) more similar, placing a larger amount of potassium conductance in the common section: the soma. The leak conductance is kept uniform all over the cell, as no physiological evidence shows any variation. The procedure is to change the distribution of K_{LVA} (and K_{HVA} accordingly) in the high frequency cell in such a way that the total conductance remains the same, namely the voltage-current relation remains unchanged. The sum of the products of the new densities by the corresponding area surfaces (dendritic and somatic) is kept constant. With the new configuration of conductances, the low frequency cell is tested.

While leaving the high frequency cell almost intact, due to its compactness, the suggested modification brings a greater amount of potassium available at the soma for the low frequency cells. In order to place enough potassium in the soma to counteract the fast sodium dynamics, the minimum ratio of conductance redistribution found is 1/4 of the original dendritic densities, and the

corresponding 4.18-fold increase in the soma. Figure 5.3 shows the voltage-current relation for the new configuration, and the corresponding time plots.

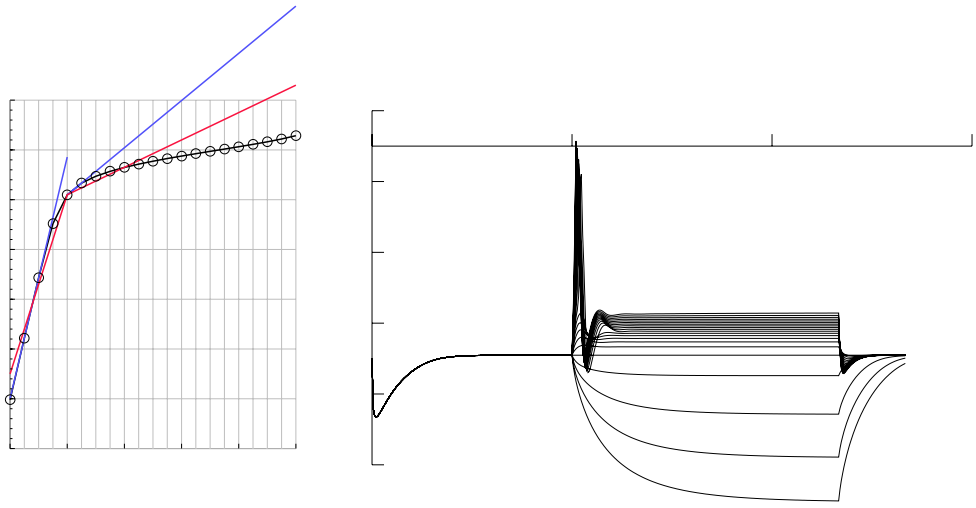

Figure 5.3: V-I plot for the 500 Hz cell after redistributing potassium conductances.

Despite bringing some degree of similarity between the two kinds of cells, there is still an important divergence that remains unaddressed. The time course of the membrane voltage is faster for the low frequency cell than for the high frequency one, which is counterintuitive and contradicts the behavior observed in real cells. Varying the ratio of conductances between the dendrites and the soma cannot solve the above-mentioned problem: in the limit, all conductances are concentrated in the soma and the two types of cells exhibit the same behavior, but the underlying phenomenon is never inverted. The mismatch in the cell's time constants is exemplified in Figure 5.4, where the voltage response to a 2 nA current clamp is plotted for a low and high frequency cell.

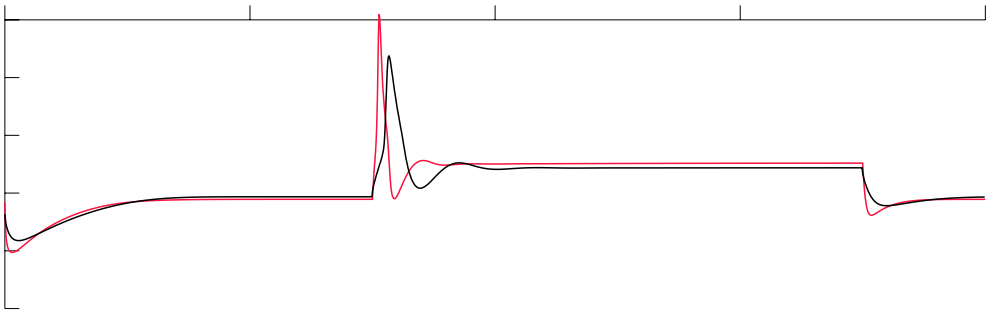

Figure 5.4: Superimposed voltage responses to a 2 nA current clamp for a low and high frequency cell.

5.3 Reshaping the dendrites

The main concern in bringing internal coherence to the model is to reproduce all the relevant features observed in real cells. Assessing the degree of relevance of each feature is mandatory to avoid introducing too much unnecessary detail and complexity into the model. For this reason, the dendrites had been initially incorporated into the model as having constant diameter both along its length and throughout the tonotopic axis of NL. Nonetheless, there is anatomical evidence that shows increased thickness of the longer dendrites at their base [9, 43, 44]. This feature is incorporated into the model and examined in the present section.

Despite the abundant evidence of the tapering of the dendritic diameter for the low frequency cells, there is no quantification available for this feature. From camera lucida reconstructions of NL cells and photomicrographs, the tapering is approximated by a fast exponential decay moving away from the soma. The tapering of the dendrites is clearly visible in low frequency cells, but is not observed in high frequency cells where the dendrites are too close to one another

to distinguish any differences in their bases. Due to the lack of evidence about in which area of nucleus laminaris the tapering starts, and the consequent difficulty in where to set the threshold for this feature, a phenomenological approximation is set by a linear regression along the tonotopic axis. At the high frequency end the tapering is absent, and progressively increases towards the caudolateral end, as described by Eq. 5.2:

$$d(x, f) = \frac{2}{3}\Big(14 - N_{den}(f)\Big)e^{-ax} + d_{min} \tag{5.2}$$

where the dendritic diameter d is a function of the position along the dendrite (x, ranging from 0 to 1) and the characteristic frequency of the cell (f). The constants are set so that the maximum dendritic diameter for the 2 dendrites case matches the minimum diameter of the soma (10 μm, cf. Section 3.1). The initial dendritic diameter is inversely proportional to the number of dendrites (N_{den} as defined in Eq. 3.5). Finally, the exponent a controls the speed of the decay. A value of about 9 for a gives a match between the voltage responses of the two cells, and an even smaller value would make the low frequency cells slower. The increased proximal dendritic surface implies a larger effective area; an increase in diameter results in a larger space constant (cf. Eq. 5.1), although the calculation is not straightforward because the diameter is no longer constant. A larger effective area implies an increase in the total leak and K_{LVA} conductances, which can counteract the fast sodium dynamics. This result shows that the tapering of the dendrites makes a great difference and thus is a relevant parameter to be incorporated into the model. However, such small values for a are not biophysically realistic: the dendrites are abnormally thick. In order to set a value for the decay coherent with anatomical and physiological observations, the slope below rest is taken as a reference and matched with the corresponding

value for the high frequency cell, because no systematic variation of this value has been observed along the tonotopic axis [36]. A value of a=20 is selected accordingly. Figure 5.5 plots the profile of the dendritic diameter along the dendritic length as specified in Eq. 5.2 (500 Hz cell, blue trace), and the corresponding segmented implementation by NEURON (red trace). Figure 5.6 shows the voltage-current relation of the low frequency cell and the corresponding time plots. Despite the still uncontrolled oscillations at higher voltages, an improvement can be seen with respect to Figure 5.2 because the oscillations appear at more positive voltages than before.

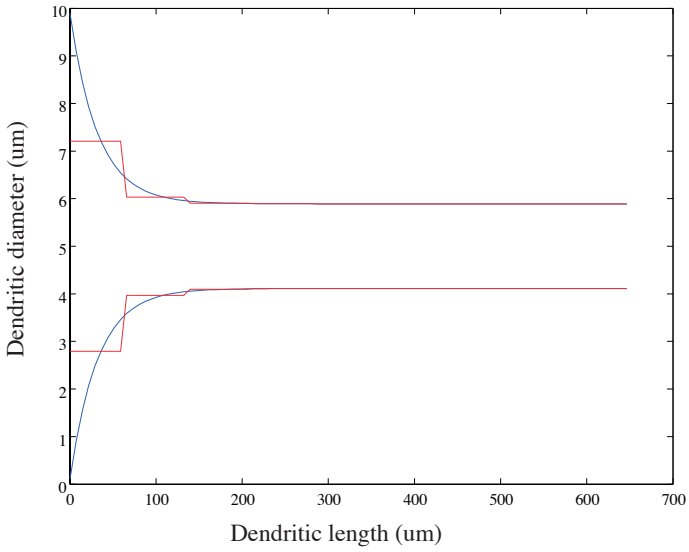

Figure 5.5: Dendritic diameter tapering along dendritic length. Comparison between the ideal profile and the segmented implementation by NEURON.

Finally, Figure 5.7 shows the two traces superimposed for the voltage response to a 2 nA current clamp for both a low and a high frequency cell. It can be observed the increase of the membrane time constant with respect to

Figure 5.4 (the conductances are kept redistributed as in the previous section to isolate the low frequency trace from secondary spikes).

5.4 Tonotopic variation of channel conductances

The morphological differences in nucleus laminaris cells is the main attributable cause of their diverse behavior. The present section discusses other variations that might be present along the tonotopic axis and could account for some questions that remain unresolved.

Physiological experiments reveal a variation in the degree of rectification between cells throughout the nucleus. No systematic variation of $R_{above\ rest}$, an estimate of the degree of rectification (cf. Section 4.1), along the tonotopic axis has been observed [36]. Nevertheless, there seems to be a trend in increasing rectification with increasing characteristic frequency of the cells (Kate MacLeod, unpublished data). Despite the different rectification ratios, both types of cells show only one single spike at the onset of currents clamps. Less rectification makes it easier for sodium channels to activate again after the initial spike and trigger secondary spikes. This can be observed in the model if the low frequency cell is implemented without the redistribution of potassium conductances analyzed in Section 5.2.

The main agent that causes the membrane voltage to oscillate around the higher clamped voltages is an excess in the density of sodium channels, which can be observed in the higher amplitudes of action potential peaks (15 mV difference between the 500 Hz cell and the 2000 Hz equivalent). In order to equilibrate potassium and sodium kinetics, one possibility is to reduce the channel density for sodium in the low frequency cells. However, simulations show that the needed

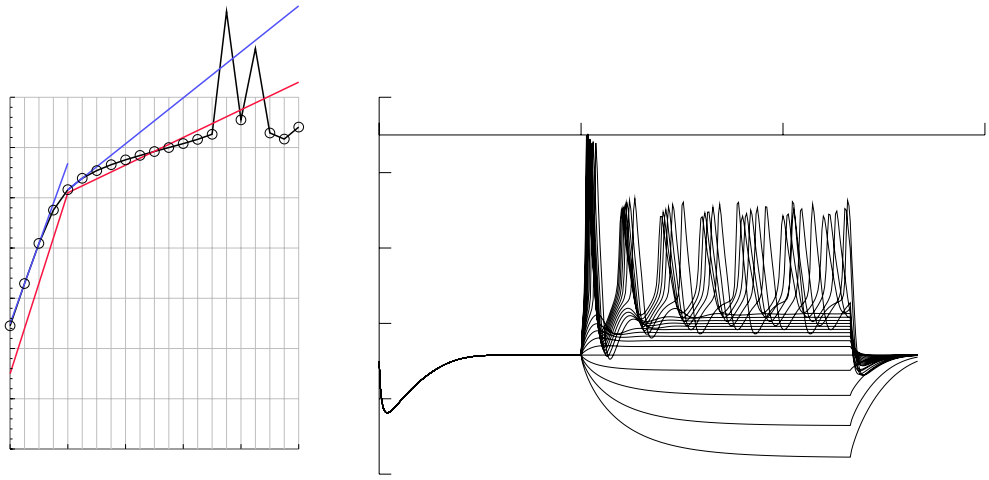

Figure 5.6: Voltage-current relation of a low frequency cell with varying diameter of the dendrites.

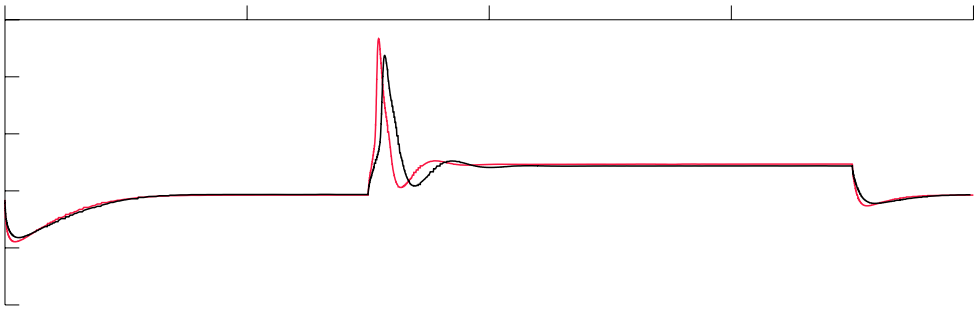

Figure 5.7: Comparison of voltage responses between a low and high frequency cell after reshaping the dendrites.

amount to eliminate unwanted oscillations is too high (70% reduction) that results in an over reduction in the spike height (5 mV below the reference for the 2000 Hz cell). Thus, a tonotopic gradient in the sodium conductance does not seem to be the main feature to counteract the anatomical differences between cells.

Among all the peculiarities of NL cells detailed in the model, there is one that is less well understood and for which changes have been kept to a minimum. K_{HVA} is thought to facilitate high frequency spiking by controling the width of the spike and quickly repolarizing the voltage to rest after the spike. However, in the high frequency cells, removing or doubling the presence of K_{HVA} does not make a substantial difference in the shape of the spike.

K_{HVA} seems to have a great influence in the low frequency cells. Removing K_{HVA} from the low frequency cells diminishes the rectification only attributed to K_{LVA}. On the other hand, increasing the presence of K_{HVA} reduces the voltage oscillations after the primary spike and helps resetting the voltage to the clamped value. Therefore, one possibility is to increase the channel densities for K_{HVA} in the low frequency cells where they have greater effect, but doing so would contradict immunoreactivity experiments that evidence higher densities in the high frequency cells of NL [29]. The fact that the present configuration of the model sets a uniform channel density for K_{HVA} along the tonotopic axis does not necessarily contradict immunoreactivity observations, as more cells with a higher number of dendrites are located in the high frequency region of NL compared to the low frequency area. Another possibility is to increase the potential effect of K_{HVA} by changing the dynamics of the channel, which have been untouched from the reference data. The idea is to increase the range of voltages in which K_{HVA}

becomes active, and/or shift the range of voltages towards the rectified voltages. Because the reference values are taken from nucleus magnocellularis, where less rectification is observed, the area of influence was shifted to more positive values. Following this reasoning, the midpoints of activation and deactivation are shifted to more negative values (from -19 to -25 mV) and the ranges of activation and deactivation are increased roughly by a 25% (α_{nk}=12 ms^{-1} and β_{nk}=25 ms^{-1}). Due to a too strong presence of sodium in the actual configuration, the mentioned feature can be better observed by either halving the sodium conductance or doubling the K_{HVA} conductance (cf. Figure 5.8). The effect of K_{HVA} can be clearly seen in eliminating oscillations at low frequencies (red and blue traces), as well as allowing a less rectified clamped voltage compared to the high frequency cell (black trace). It is important to mention that such a change does not cause significant alterations in the voltage response in the high frequency cell, and it thus applied uniformly to all cells.

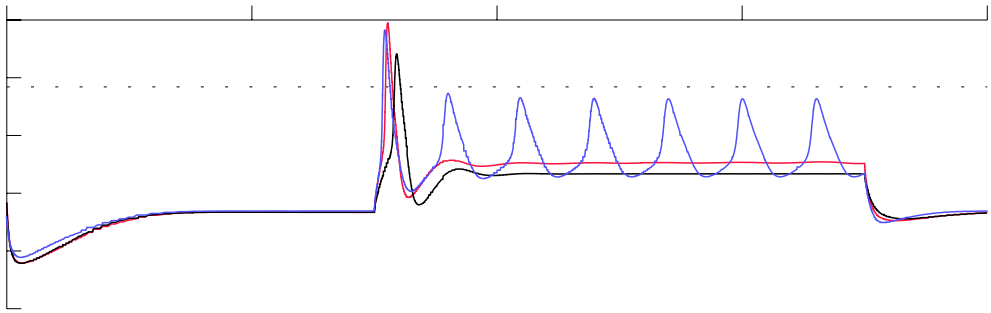

Figure 5.8: Comparison of voltage responses between a low (red) and a high (black) frequency cell while assessing the effect of K_{HVA}. The blue trace shows the reference setting for K_{HVA} in the low frequency cell.

Chapter 6

Conclusions

The aim of the present work has been to improve an existing computational model of nucleus laminaris to make it biophysically more realistic, where special interest is drawn towards the tonotopic arrangement of NL cells. The starting point for characterizing NL cells is the high frequency region of the nucleus, from where most of the biological data is derived. The degree of accuracy sought in the present model implies a high number of parameters that define an intractably huge space of possible combinations. The approach to find where the biologically relevant subspace lies has been to combine the experimental data available in the literature with an exhaustive distributed exploration of the variable space.

Whereas the variable space for the low voltage activated potassium channels seems quite compact, the relevant subspace for sodium remains hard to delimitate mostly because of its higher dimensionality. Interacting in the same voltage range as sodium, high voltage activated potassium channels have not been precisely studied due to the lack of biological constraints.

Having faithfully characterized an average high frequency cell, its main features are adapted to the low frequency region to provide with a description of the behavior of the entire nucleus laminaris. The morphological variations along

the tonotopic axis reported in the literature constitute the framework for studying both types of cells (2000 Hz and 500 Hz cells). Important unexpected physiological divergences are observed in the low frequency cells. The counterintuitive disparities between both cell types are studied by introducing physiological modifications that might correct the observed phenomena. Such modifications include a redistribution of conductances between the soma and the dendrites, and tonotopic gradients of conductances.

None of the physiological modifications proposed can account for the disparity between the model and real cells in the low frequency region. Only anatomical adaptations can indeed give a partial explanation, although they have to be pushed away from biological limits to fully resolve the observed paradox: low frequency cells are faster than the high frequency analogous. The particular morphological configuration of the cells seems to have an underestimated effect on their behavior. A more accurate description of the anatomy of these neurons is needed to complete the model.

Deriving from the attained biological accuracy in the model, a new functionality of high potassium activated channels is hypothesized for the low frequency cells. In the most caudal cells where less rectification is observed, K_{HVA} is thought to help repolarization complementing the effect of a less dense low threshold activated conductance.

BIBLIOGRAPHY

[1] Agmon-Snir, H., Carr, C. E., and Rinzel, J. (1998) The role of dendrites in auditory coincidence detection. *Nature.* **393**: 268–272.

[2] Carr, C. E., and Boudreau, R. E. (1993) An axon with a myelinated initial segment in the bird auditory system. *Brain Res.* **628**: 330–334.

[3] Carr, C. E., and Konishi, M. (1990) A circuit for detection of interaural time differences in the brain stem of the barn owl. *J. Neurosci.* **10**(10): 3227–3246.

[4] Carr, C. E., Soares, D., Parameshwaran, S., and Perney, T. (2001) Evolution and development of time coding systems. *Curr. Opin. Neurobiol.* **11**(6): 727–733.

[5] Colbert, C. M., and Pan, E. (2002) Ion channel properties underlying axonal action potential initiation in pyramidal neurons. *Nat. Neurosci.* **5**(6): 533–538.

[6] Cook, D. L., Schwindt, P. C., Grande, L. A., and Spain, W. J. (2003) Synaptic depression in the localization of sound. *Nature.* **421**: 66–70.

[7] Crill, W. E. (1996) Persistent sodium current in mammalian central neurons. *Ann. Rev. Physiol.* **58**: 349–362.

[8] Cummins, T. R., Xia, Y., and Haddad, G. G. (1994) Functional properties of rat and human neocortical voltage-sensitive sodium currents. *J. Neurophysiol.* **71**: 1052–1064.

[9] Deitch, J. S., and Rubel, E. W. (1984) Afferent influences on brain stem auditory nuclei of the chicken: time course and specificity of dendritic atrophy following deafferentation. *J. Comp. Neurol.* **229**(1): 66–79.

[10] Deitch, J. S., and Rubel, E. W. (1989) Changes in neuronal cell bodies in n. laminaris during deafferentation-induced dendritic atrophy. *J. Comp. Neur.* **281**: 259–268.

[11] Deitch, J. S., and Rubel, E. W. (1989) Rapid changes in ultrastructure during deafferentation-induced dendritic atrophy. *J. Comp. Neur.* **281**: 234–258.

[12] Hille, B. (2001) *Ion channels of excitable membranes*, 3rd edition. Sunderland, MA: Sinauer Associates.

[13] Hines, M. L. (1983) Efficient computation of branched nerve equations. *Int. J. Bio-Med. Comput.* **15**(1): 69–76.

[14] Hines, M. L., and Carnevale, N. T. (1997) The NEURON simulation environment. *Neural Comput.* **9**(6): 1179–1209.

[15] Hines, M. L., and Carnevale, N. T. (2000) Expanding NEURON's repertoire of mechanisms with NMODL. *Neural Comput.* **12**(5): 995–1007.

[16] Hines, M. L., and Carnevale, N. T. (2001) NEURON: a tool for neuroscientists. *Neuroscientist.* **7**(2): 123–135.

[17] Hodgkin, A. L., and Huxley, A. F. (1952) A quantitative description of membrane current and its application of conduction and excitation in nerve. *J. Physiol. Lond.* **117**: 500–544.

[18] Jeffress, L. A. (1948) A place theory of sound localization. *J. Comp. Physiol. Psychol.* **41**: 35–39.

[19] Johnston, D., and Wu, S. M. (1999) *Foundations of cellular neurophysiology*, 4th edition. Cambridge, MA: The MIT Press.

[20] Kernighan, B. R., and Pike, R. (1984) Appendix 2: Hoc manual. In: *The UNIX programming environment.* Englewood Cliffs: NJ: Prentice-Hall, pp. 329–333.

[21] Koch, C. (1999) *Biophysics of computation.* New York: Oxford University Press.

[22] Koyano, K., Funabiki, K., and Ohmori, H. (1996) Voltage-gated ionic currents and their roles in timing coding in auditory neurons of the nucleus magnocellularis of the chick. *Neurosci. Res.* **26**(1): 29–45.

[23] Kuba, H., Koyano, K., and Ohmori, H. (2002) Development of membrane conductances improves coincidence detection in the nucleus laminaris of the chicken. *J. Physiol.* **540**(2): 529–42.

[24] Lytton, W. W., and Sejnowski, T. J. (1991) Simulations of cortical pyramidal neurons synchronized by inhibitory interneurons. *J. Neurophysiol.* **66**(3): 1059–1079.

[25] Martina, M., and Jonas, P. (1997) Functional differences in Na+ channel gating between fast spiking interneurones and principal neurones of rat hippocampus. *J. Physiol.* **505**(3): 593–603.

[26] Moore, J. W., Joyner, R. W., Brill, M. H., Waxman, S. D., and Najar-Joa, M. (1978) Simulations of conduction in uniform myelinated fibers. *J. Biophys.* **21**: 147–160.

[27] Oertel, D. (1999) The role of timing in the brain stem auditory nuclei of vertebrates. *Annu. Rev. Physiol.* **61**: 497–519.

[28] Overholt, E. M., Rubel, E. W., and Hyson, R. L. (1992) A circuit for coding interaural time differences in the chick brainstem. *J. Neurosci.* **12**(5): 1968–1708.

[29] Parameshwaran, S., Carr, C. E., and Perney, T. M. (2001) Expression of the Kv3.1 potassium channel in the avian auditory brainstem. *J. Neurosci.* **21**(2): 485–494.

[30] Parks, T. N., Collins, P., and Conlee, J. W. (1983) Morphology and origin of axonal endings in nucleus laminaris of the chicken. *J. Comp. Neur.* **214**: 32–42.

[31] Peters, A., Palay, S. L., and Webster, H. D. (1991) *The fine structure of the nervous system*, 3rd edition. New York: Oxford University Press.

[32] Protopapas, A. D., Vanier, M., and Bower, J. M. (1999) Simulating large networks of neurons. In: *Methods in neuronal modeling*. Koch, C., and Segev, I., editors. Cambridge, MA: The MIT Press, pp. 461–498, 2nd edition.

[33] Rall, W. (1959) Branching dendritic trees and motoneuron membrane resistivity. *Exp. Neurol.* **1**: 491–527.

[34] Rathouz, M., and Trussell, L. (1998) Characterization of outward currents in neurons of the avian nucleus magnocellularis. *J. Neurophysiol.* **80**(6): 2824–35.

[35] Reyes, A. D., Rubel, E. W., and Spain, W. J. (1994) Membrane properties underlying the firing of neurons in the avian cochlear nucleus. *J. Neurosci.* **14**(9): 5352–5364.

[36] Reyes, A. D., Rubel, E. W., and Spain, W. J. (1996) In vitro analysis of optimal stimuli for phase-locking and time-delayed modulation of firing in avian nucleus laminaris neurons. *J. Neurosci.* **16**(3): 993–1007.

[37] Rogart, R. B., and Ritchie, J. M. (1977) Physiological basis of conduction in myelinated nerve fibers. In: *Myelin*. Morell, P., editor. New York: Plenum Press, pp. 117–160.

[38] Rubel, E. W., and Parks, T. N. (1975) Organization and development of brain stem auditory nuclei of the chicken: tonotopic organization of n. magnocellularis and n. laminaris. *J. Comp. Neur.* **164**: 411–434.

[39] Rubel, E. W., and Parks, T. N. (1988) Organization and development of the avian brain-stem auditory system. In: *Auditory function: neurobiological bases of hearing*. Edelman, G. M., Gall, W. E., and Cowan, W. M., editors. New York: Wiley Press, pp. 3–92.

[40] Rudy, B., and McBain, C. J. (2001) Kv3 channels: voltage-gated K+ channels designed for high-frequency repetitive firing. *Trends Neurosci.* **24**(9): 517–526.

[41] Schwarz, J. R., and Eikhof, G. (1987) Na currents and action potentials in rat myelinated nerve fibres at 20 and 37 degrees C. *Pflugers Arch.* **409**(6): 569–577.

[42] Simon, J. Z., Carr, C. E., and Shamma, S. A. (1999) A dendritic model of coincidence detection in the avian brainstem. *Neurocomputing*. **26-27**: 263–269.

[43] Smith, D. J. (1981) Organization and development of brain stem auditory nuclei of the chicken: dendritic development in n. laminaris. *J. Comp. Neur.* **203**: 309–333.

[44] Smith, D. J., and Rubel, E. W. (1979) Organization and development of brain stem auditory nuclei of the chicken: dendritic gradients in nucleus laminaris. *J. Comp. Neur.* **186**: 213–240.

[45] Svirskis, G., Kotak, V., and Rinzel, J. (2002) Enhancement of signal-to-noise ratio and phase locking for small inputs by a low-threshold outward current in auditory neurons. *J. Neurosci.* **22**(24): 11019–11025.

[46] Traub, R. D., Wong, R. K. S., Miles, R., and Michelson, H. (1991) A model of a CA3 hippocampal pyramidal neuron incorporating voltage-clamp data on intrinsic conductances. *J. Neurophysiol.* **66**: 635–650.

[47] Warchol, M. E., and Dallos, P. (1990) Neural coding in the chick cochlear nucleus. *J. Comp. Physiol.* **166**: 721–734.

[48] Yamada, W. M., Koch, C., and Adams, P. R. (1999) Multiple channels and calcium dynamics. In: *Methods in neuronal modeling*. Koch, C., and Segev, I., editors. Cambridge, MA: The MIT Press, pp. 137–170, 2nd edition.

[49] Zhang, S., and Trussell, L. O. (1994) A characterization of excitatory postsynaptic potentials in the avian nucleus magnocellularis. *J. Neurophysiol.* **72**(2): 705–718.

[50] Zhang, S., and Trussell, L. O. (1994) Voltage clamp analysis of excitatory synaptic transmission in the avian nucleus magnocellularis. *J. Physiol.* **480**(1): 123–136.